Contract F49620-88-C-0037

MCR 90-513

AD-A227 276

Final Report

AFOSR-TR- 90 1031

June 1990

Large Space Manipulators Study

DTIC FILE COPY

DTIC
ELECTE
SEP 23 1990
D

DISTRIBUTION STATEMENT A
Approved for public release;
Distribution Unlimited

MARTIN MARIETTA

Contract F49620-88-C-0037

Final
Report — June 1990

Large Space Manipulators Study

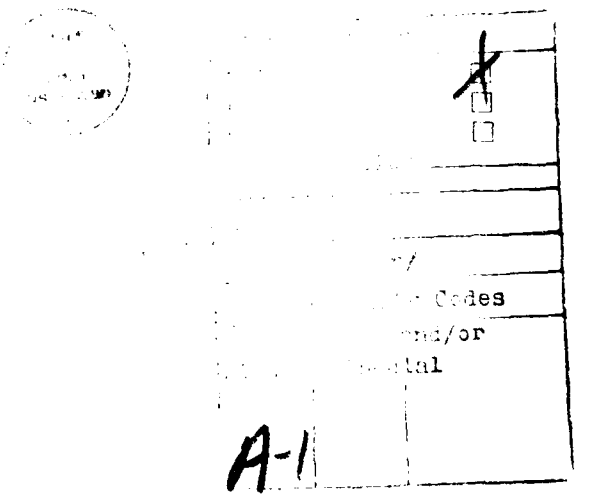

MARTIN MARIETTA
ASTRONAUTICS GROUP
P. O. Box 179
Denver, Colorado 80201

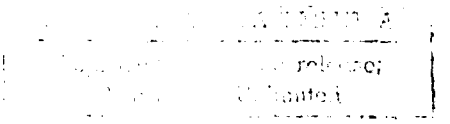

(U)

SECURITY CLASSIFICATION OF THIS PAGE

REPORT DOCUMENTATION PAGE

1a. REPORT SECURITY CLASSIFICATION	1b. RESTRICTIVE MARKINGS
2a. SECURITY CLASSIFICATION AUTHORITY	3. DISTRIBUTION / AVAILABILITY OF REPORT Approved for public release, distribution unlimited
2b. DECLASSIFICATION / DOWNGRADING SCHEDULE	
4. PERFORMING ORGANIZATION REPORT NUMBER(S)	5. MONITORING ORGANIZATION REPORT NUMBER(S)
6a. NAME OF PERFORMING ORGANIZATION Martin Marietta Space Systems Co. Research & Technology Dept.	6b. OFFICE SYMBOL (If applicable)
	7a. NAME OF MONITORING ORGANIZATION Air Force Office of Scientific Research
6c. ADDRESS (City, State, and ZIP Code) P.O. Box 179 M/S 4372 Denver, CO 80201	7b. ADDRESS (City, State, and ZIP Code) Bolling Air Force Base, Bldg. 410 DC 20332-6448
8a. NAME OF FUNDING / SPONSORING ORGANIZATION Strategic Defense Initiative Org.	8b. OFFICE SYMBOL (If applicable) SDIO
	9. PROCUREMENT INSTRUMENT IDENTIFICATION NUMBER F 49620-88-C-0037
8c. ADDRESS (City, State, and ZIP Code) Department of Defense Washington, DC 20301-7100 NA	10. SOURCE OF FUNDING NUMBERS PROGRAM ELEMENT NO. 61102F; PROJECT NO. 2312; TASK NO. A1; WORK UNIT ACCESSION NO.
11. TITLE (Include Security Classification) Final report, Large Space Manipulators Study (U)	
12. PERSONAL AUTHOR(S) Eric Schmitz (Principal Investigator) and Madison Ramey	
13a. TYPE OF REPORT Final	13b. TIME COVERED FROM 5/88 TO 5/90
14. DATE OF REPORT (Year, Month, Day) 1990 June	15. PAGE COUNT
16. SUPPLEMENTARY NOTATION	

17 COSATI CODES		
FIELD	GROUP	SUB-GROUP

18. SUBJECT TERMS (Continue on reverse if necessary and identify by block number)
Large Space Structures, Long-reach Space Robots, Nonlinear Dynamics of Elastic, Articulated Structures, Active Control, Control/Structures./Interaction, Vibration Control

19. ABSTRACT (Continue on reverse if necessary and identify by block number)

- See Next Page -

20. DISTRIBUTION / AVAILABILITY OF ABSTRACT ☑ UNCLASSIFIED/UNLIMITED ☑ SAME AS RPT. ☑ DTIC USERS	21. ABSTRACT SECURITY CLASSIFICATION (U)
22a. NAME OF RESPONSIBLE INDIVIDUAL Lt. Col. G.K. Haritos	22b. TELEPHONE (Include Area Code) (202) 767-4987
	22c. OFFICE SYMBOL AFOSR

DD FORM 1473, 84 MAR 83 APR edition may be used until exhausted. All other editions are obsolete.

SECURITY CLASSIFICATION OF THIS PAGE

(U)

Abstract

This report documents the research performed for the "Large Space Manipulator Study" contract. The derivation of nonlinear dynamic models for a simple 3-D articulated, elastic structure is discussed. Kane's dynamics equations are used to obtain equations of motion in closed form; the bending deformations of the elastic links, modelled as slender elastic beams, are described with the assumed-modes method. A 2-D planar version of the dynamic model is used to predict the dynamic behavior of an experimental, articulated two-link elastic structure. Both links consist of thin elastic beams with rectangular cross section. The outer link has a tip payload of variable mass and moment of inertia. The structure is instrumented with position/rate/acceleration sensors mounted at the articulations and at the end-point; strain-gauges are mounted along the links at several locations. Close agreement between the analytical predictions and the experimental measurements is documented for modal tests and for slew maneuvers of the structure. The design and implementation of several digital compensators to actively control the single elastic beam as well as the 2-DOF elastic structure are presented. The compensators are obtained using classical design techniques and the Linear Quadratic Gaussian/Loop Transfer Recovery (LQG/LTR) method.

CONTENTS

Page

1 Introduction **1-1**

1.1 Rationale for the Research 1-1

1.2 Research Objectives 1-2

2 Dynamic Models of Articulated Elastic Structures **2-1**

2.1 Introduction 2-1

2.2 General Method of Derivation 2-1

2.3 Dynamic Models for the 2-D Elastic Articulated Structure 2-4

2.3.1 Choice of Mode Shapes for 2-D Dynamic Model 2-6

2.3.2 Experimental Validation of the Linearized Models 2-8

2.3.3 Experimental Validation of the Nonlinear Dynamic Models . . . 2-10

2.4 Conclusion 2-13

3 Control Law Designs and Implementations **3-1**

3.1 Single Link Active Modal Control 3-1

3.1.1 LQG/LTR Controller Design Method 3-2

3.1.2 Experimental Results 3-5

3.1.3 Parameter Robust LQG/LTR Design 3-6

3.2 Rigid-Flex Control 3-10

3.3 Flex-Flex Control 3-10

3.3.1 Regulator Designs 3-11

3.3.2 Estimator Designs 3-16

3.4 Conclusions 3-18

A Personnel and Interactions with Research Community **A-1**

A.1 Personnel A-1

A.2 Papers Presented at Conferences A-1

A.3 Interactions A-2

B APPENDIX: Simplified Mass and Stiffness Matrices for 3-D Elastic Structure **B-1**

B.1 Kinematics B-1

B.2 Linearized Partial Velocities B-3

B.3 Mass Matrix $\overline{M}(X_r)$ B-4

B.3.1 Submatrix $\overline{M}_{RE}$ B-4

B.3.2 Submatrix $\overline{M}_{EE}$ B-5

B.4 Stiffness Matrix K_{EE} B-6

C MATRIXx UDF's and Control Law Subroutines **C-1**

C.1 LQG Design and Analysis UDF's C-1

C.2 Real-Time Controller Module C-5

Chapter 1

Introduction

The report documents the research accomplishments for the first two years of a three-year program titled "Large Space Manipulators Study". Due to budget constraints, the third year of this contract was not funded. This program is sponsored by the Strategic Defense Initiative Organization (SDIO) and managed by the Air Force Office of Scientific Research (AFOSR). This section of the report outlines the rationale and the specific objectives of the research effort.

1.1 Rationale for the Research

Design of algorithms for rapid large angle slew maneuvers and vibration supression of space structures modelled as articulated chains of elastic bodies is a key technology issue for the SDIO mission. Example of such structures are (1) large space manipulators and (2) space-based lasers (SBL). In the first case, manipulators such as the Remote Manipulator System (RMS) are characterized by two main long links which behave as slender elastic beams with significant bending and torsional compliance. The fundamental vibration frequency of the RMS is very low, typically in the range of 0.05 to 0.5 Hz depending on the mass of the payload. It is expected that long-reach manipulators, used in concert with small dexterous manipulators, will play a key role for the satellite servicing activities related to the SDI mission. In the later case, SBL are typically modelled as truss-like elastic structures hinged to large rigid platforms. Standard linear models derived from finite-element codes used by the Large Space Structures (LSS) control community are not adequate to predict the dynamic behavior of this class of elastic structures. Dynamic models which account for the geometric nonlinearities due to large angle motions occuring at the articulations need to be developed. Control techniques for the slewing and pointing of such structures can then be studied based on these nonlinear dynamic models. A sequence of control laws need to be developed from simple linear feedback laws using colocated sensor/actuator pairs to nonlinear controllers compensating for the nonlinear coupled dynamics.

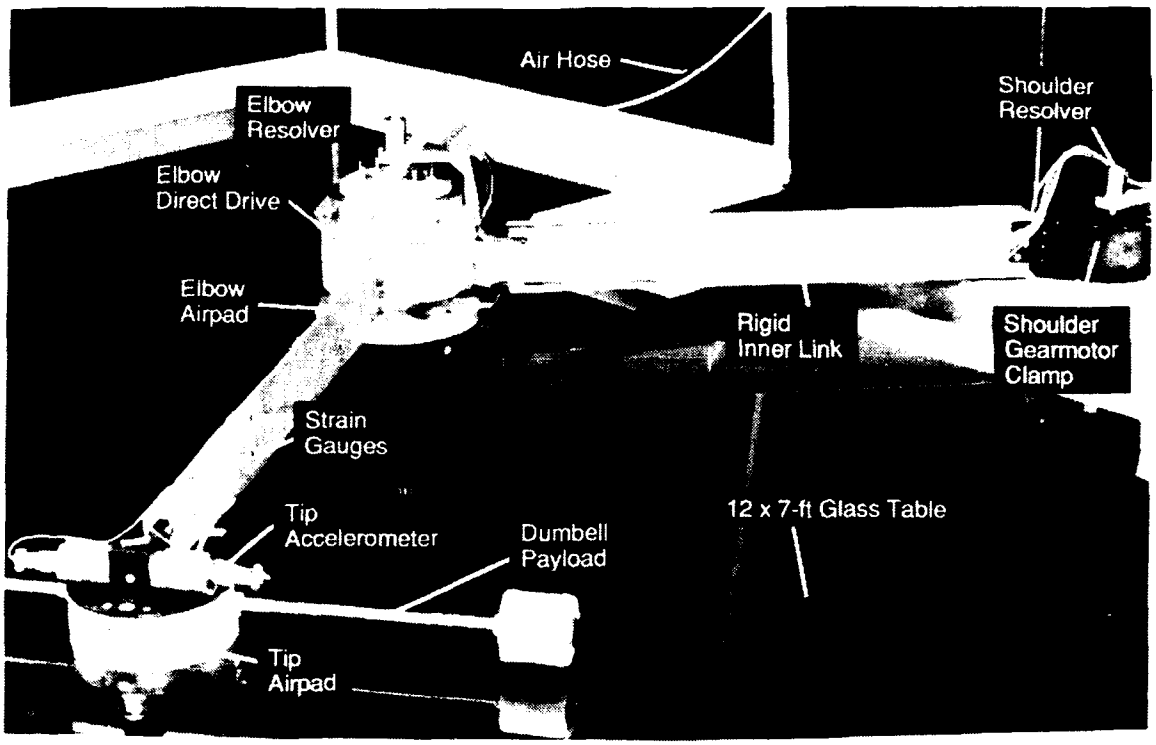

Figure 1-1: Experimental 2D articulated structure

1.2 Research Objectives

The research performed under this program is a combination of theoretical and experimental investigations. Central to this research is an experimental testbed for a planar $2D$ articulated elastic structure. The testbed shown in Figure 1 has a fundamental vibration frequency in the range of 0.5 Hz to 1.5 Hz, depending on the particular links/payload configuration. The testbed is used both for dynamic model validation as well as for demonstration of various control strategies.

The specific research objectives for the original three year program as outlined in the statement of work are given below:

- Develop a detailed dynamic mathematical model for a representative three-dimensional elastic, articulated structure.
- Design and implement a series of compensators for a laboratory model of an articulated elastic structure moving in the horizontal plane.
- Develop concepts for a nonlinear control law applied to the elastic planar manipulator testbed.
- Study the feasability of implementing advanced control concepts developed by

other investigators on the experimental testbed.

- Extend advanced control concepts to fully three-dimensional space structure implementations.

The next two sections of the report documents the progress made in accomplishing the research objectives during the first two years of the contract. Appendix A lists the professional personnel associated with the research and the interactions (coupling activities) performed in the context of this contract.

Chapter 2

Dynamic Models of Articulated Elastic Structures

2.1 Introduction

The goal of this task is (1) to derive equations of motion in closed form for articulated chains of elastic bodies (2-D and 3-D) and (2) to validate the corresponding dynamic models against experimental data for the case of a planar testbed.

The generic articulated structure studied here is shown in Figure 2-1. The first body (shoulder joint) is rigid and the two main links are modelled as slender elastic beams which can bend in two orthogonal directions. A rigid "payload" is cantilevered at the tip of the second link. The three joint angles (θ_1, θ_2, θ_3) can take arbitrarily large values. Three torque actuators are located at the joints. A 2-D version of the test structure is obtained by locking the first joint θ_1; in this case, the plane of motion is orthogonal to the joint axes 2 and 3 (only the elastic deformations in that plane are considered). The experimental testbed shown in Figure 2-2 has been designed to emulate the 2-D planar version of the articulated structure.

In Section 2.2 we review the general method of derivation based on Kane's equations. The simplified nonlinear mass matrix and stiffness matrix for the 3-D articulated structure are described in Appendix B. In Section 2.3 we briefly describe the three dynamic simulation models coded for the planar elastic structure. We also discuss the selection of the assumed mode shapes. Finally we document the experimental validations of the linearized and the nonlinear analytical models.

2.2 General Method of Derivation

The equations of motion for the elastic articulated structure described above are obtained using Kane's method. The first step in the derivation is to replace the distributed

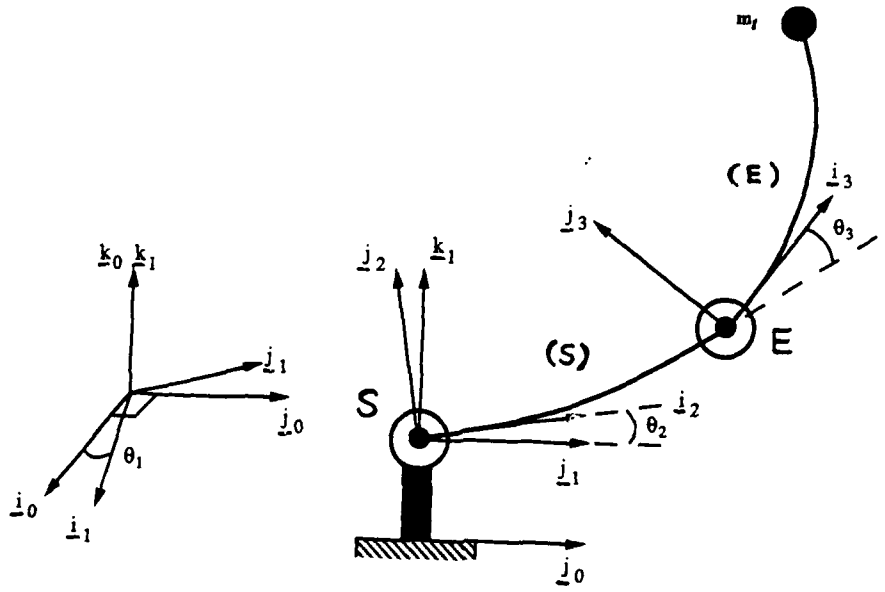

Figure 2-1: Schematic of the 3-D flexible articulated structure: the two main links are modelled as slender elastic beams with uniform mass properties. Lumped masses at the tip of the inner and outer beams represent the elbow joint drive and the tip payload respectively.

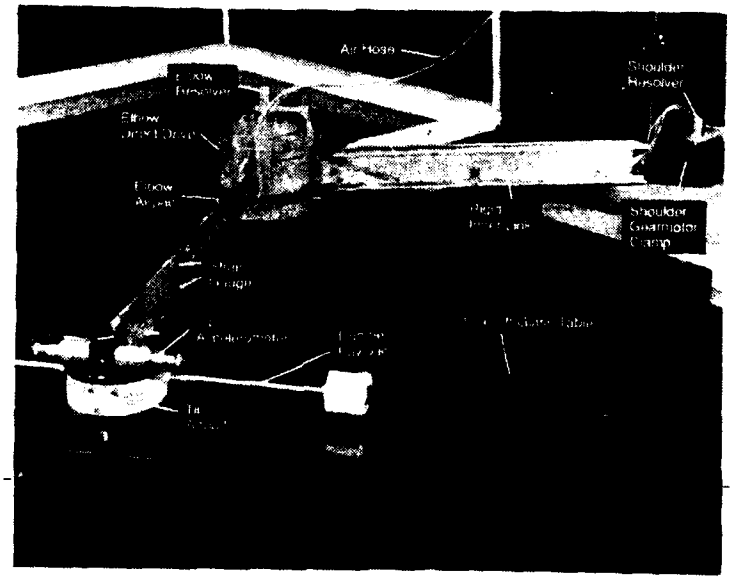

Figure 2-2: Photograph of the Experimental Flexible Manipulator (shown here in a rigid-flex configuration)

elastic coordinates for each elastic body by a finite series of the form

$$\mathbf{v}(\mathbf{x},\mathbf{t}) = \sum_{\mathbf{i}=1}^{\mathbf{n}} \mathbf{\Phi_i}(\mathbf{x})\mathbf{q_i}(\mathbf{t}) \qquad (2-1)$$

where the "assumed" mode shapes $\mathbf{\Phi_i}(\mathbf{x})$ form a set of admissible functions satisfying the geometric boundary conditions for the elastic deflections. The issue of the selection of the assumed mode shapes is discussed in the next section. The time-dependent coordinates $q_i(t)$ are now new generalized coordinates for the problem. The state vector X is then defined as $[X_r, X_{el}]$ where X_r consists of the 3 rigid-body coordinates $\theta_i(t)$ and X_{el} consists of nt elastic coordinates $q_i(t)$.

Using any derivation method, Lagrange, Newton or Kane's, the equations of motion for the elastic structure will be of the form:

$$M(X)\ddot{X} + D\dot{X} + KX = G\mathbf{U} + \mathbf{T_{nlin}}(\mathbf{X},\dot{\mathbf{X}}) \qquad (2-2)$$

where $M(X)$ is the configuration-dependent mass matrix, D and K are respectively the damping and the stiffness matrices for the composite elastic structure, $\mathbf{T_{nlin}}(\mathbf{X},\dot{\mathbf{X}})$ are the nonlinear torques arising from the centrifugal and Coriolis forces, G is the control distribution matrix and U is a 3 by 1 vector of actuator torques. This formulation implicitely assumes that *linear* elasticity theory is used to describe the structural deformations of the elastic bodies; consequently, the terms of order X_{el}^2 which may appear in course of the derivation of equation (2-2) should not be included. As we discussed already in [2], the mass and stiffness matrix can be expressed as:

$$M(X) = \overline{M}(X_r) + \tilde{M}(X_r, X_{el}) \qquad (2\text{-}3)$$

$$\mathbf{T_{nlin}}(\mathbf{X},\dot{\mathbf{X}}) = \overline{\mathbf{T}}_{nlin}(X_r,\dot{X}_r) + \tilde{\mathbf{T}}_{nlin}(X,\dot{X}) \qquad (2\text{-}4)$$

where the terms with the superscript $\bar{}$ depend only on the rigid coordinates X_r while the ones with the superscript $\tilde{}$ are linear in the elastic coordinates X_{el} and/or in the time-derivatives $\dot{X}_{el}$.

A *simplified* dynamic model is obtained by evaluating the terms dependent only on the rigid coordinates,i.e., the mass matrix $\overline{M}(X_r)$ and the nonlinear torques $\overline{\mathbf{T}}_{nlin}(X_r,\dot{X}_r)$ which are both zeroth-order in X_{el}. Such a model is much easier to derive than the complete model. As discussed in the next section, comparisons with the experimental data obtained with the planar testbed have shown (so far) that the simplified model is sufficient to accurately predict the rigid/elastic dynamic effects.

There are no real theoretical difficulties in deriving analytical expressions for each term of (2-2). The matrices K, D and G are readily obtained as constant matrices derived

from the assumed mode shapes $\Phi_i(x)$ selected for each elastic body. The main challenge is in the time-consuming, error-prone derivations required to compute the elements of the mass matrix $M(X)$ and of the vector of nonlinear torques T_{nlin}. In contrast to Lagrange's method, Kane's method enables the analyst to compute each of these terms *independently* and using only simple vectorial operations. If M_i is a generic point along link i, the linear velocity V_{M_i} and acceleration A_{M_i} of M_i can be expressed as:

$$\mathbf{V}_{\mathbf{M_i}} = \mathbf{G}_{\mathbf{M_i}}\dot{\mathbf{X}} \tag{2-5}$$

$$\mathbf{A}_{\mathbf{M_i}} = \mathbf{G}_{\mathbf{M_i}}\ddot{\mathbf{X}} + \dot{\mathbf{X}}^{\mathbf{T}}\frac{\partial \mathbf{G}_{\mathbf{M_i}}}{\partial \mathbf{X}}\dot{\mathbf{X}} \tag{2-6}$$

The row vector $\mathbf{G}_{\mathbf{M_i}}$ of N partial velocities $\mathbf{V}^{\mathbf{r}}_{\mathbf{M_i}}$ and the $N \times N$ matrix $\mathbf{H} = \frac{\partial \mathbf{G}_{\mathbf{M_i}}}{\partial \mathbf{X}}$ are obtained solely from expressions based on elementary differential geometry.

Having derived the partial velocities vector $\mathbf{V}^{\mathbf{r}}{}_{\mathbf{M_i}}$, the mass matrix $M(X)$ is then simply obtained as:

$$m_{rs} = \sum_i \int_{B_i} \mathbf{V}^{\mathbf{r}}_{\mathbf{M_i}} \cdot \mathbf{V}^{\mathbf{s}}_{\mathbf{M_i}} \mathbf{dm} \tag{2-7}$$

Conversely, the nonlinear torques $\mathbf{T}_{\mathbf{nlin}}(\mathbf{X}, \dot{\mathbf{X}})$ are expressed as:

$$\mathbf{T}^{\mathbf{r}}_{\mathbf{nlin}}(\mathbf{X}, \dot{\mathbf{X}}) = \sum_i \dot{\mathbf{X}}^{\mathbf{T}} \left[\int_{\mathbf{B_i}} \mathbf{H}_{\mathbf{M_i}} \cdot \mathbf{V}^{\mathbf{r}}_{\mathbf{M_i}} \mathbf{dm} \right] \dot{\mathbf{X}} \tag{2-8}$$

where the dot product involves each vector element of the matrix $\mathbf{H}_{\mathbf{M_i}}$ with $\mathbf{V}^{\mathbf{r}}_{\mathbf{M_i}}$.

These calculations involving only dot products and partial differentiation of vectors are much easier to perform than the lengthy derivations of the Lagrange method. In Appendix B we illustrate the main steps in the derivation of the simplified mass matrix $\overline{M}(X_r)$ and of the stiffness matrix K for the 3-D elastic structure described above.

2.3 Dynamic Models for the 2-D Elastic Articulated Structure

Figure 2-3 shows a schematic of the planar structure. Each link is modelled as an Euler-Bernouilli slender elastic beam with rigid inertias at each end. The testbed has been used in three different configurations: (1) single elastic link, (2) 2-DOF rigid-flex arm where the inner link is rigid and (3) 2-DOF flex-flex arm where both links are flexible.

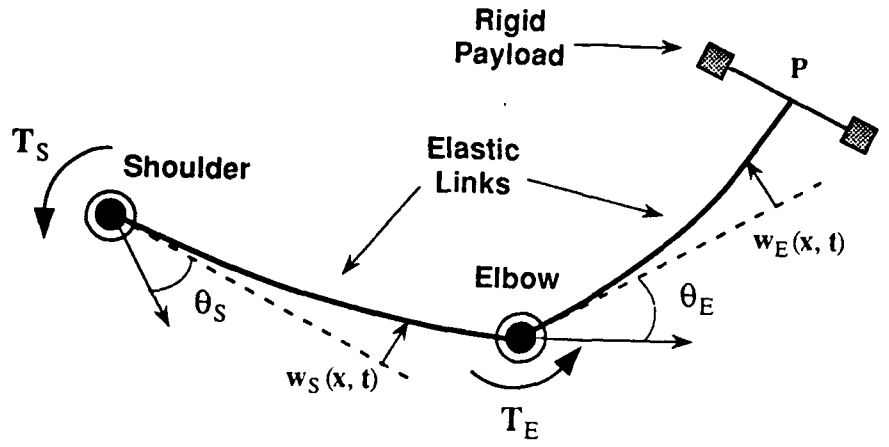

Figure 2-3: Schematic of planar elastic arm

Accordingly three different simulations have been developed for model validation and control designs. All the simulations have been coded using the System-Build simulation tool of the MATRIXx CAD software [14]. The MATRIXx software provides a convenient environment for control design, simulation and comparison with the experimental data.

The first simulation is a single elastic link model. In this case, the rigid/elastic dynamics are written in modal form. The coefficients of the state-space model (frequencies and mode shapes) are obtained from a user-defined function in MATLAB [13]; this code solves for the (exact) system frequencies and mode shapes of a composite elastic beam pinned at one end and loaded by a rigid inertia at the other end. The linear state-space model used for control design and validation is typically 8th-order with one rigid-body mode and the first three elastic modes. The simulation includes also a general analog or discrete linear compensator model, a simple nonlinear model for the Coulomb friction and simple filters to represent the sensors dynamics as shown in the block diagram of Fig. 2-4.

The second simulation is a nonlinear dynamic model of the 2-D structure with an inner rigid link and an outer elastic link. A complete model including the foreshortening effects due to kinematic nonlinearities has been described in [2]. A simplified model,where all the terms involving the elastic coordinates in the mass matrix and in the nonlinear torques are eliminated, has also been developed.

Finally the third simulation is a nonlinear dynamic model of the 2-D structure with both links flexible. The code was developed by C. Padilla and is documented in [5]. The user can select either the complete model including all the first-order terms dependent on

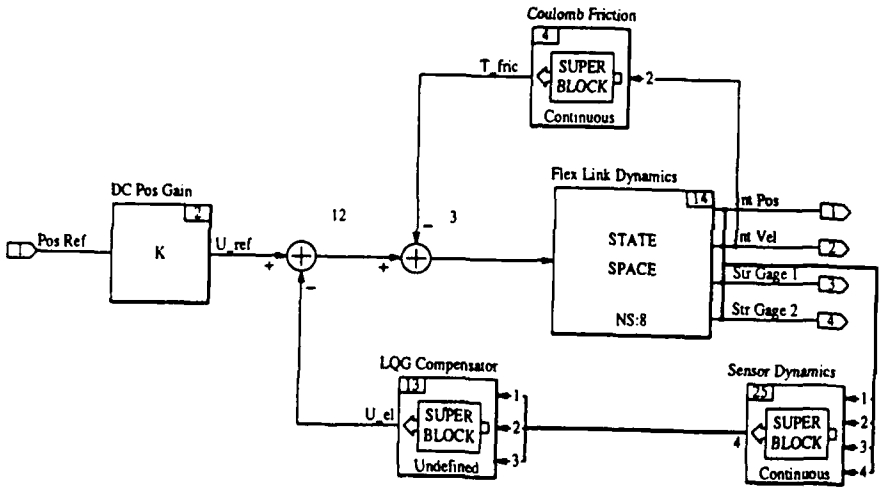

Figure 2-4: Simulation Block Diagram for the Single Elastic Link Linear Dynamic Model

the elastic coordinates, or the simplified model where these terms are neglected. As done for the single link simulation, actuator and sensor dynamic models are included together with the compensator model (discrete or analog) as shown in Fig. 2-5.

2.3.1 Choice of Mode Shapes for 2-D Dynamic Model

We discuss here the issue of mode shapes selection for the arm in the flex-flex configuration. The assumed mode shapes chosen for each link are the cantilevered modes $\phi_i^c(x)$ of a uniform elastic beam with a rigid tip body. Using the mode shapes of a loaded beam allows for transmission of shear force and bending moment at the elbow joint. In the finite-element litterature, these modes are sometimes referred as "loaded-interface modes". As shown in Figure 2-3, the cantilevered boundary conditions are compatible with the particular choice of the frame of reference in which the elastic deflections are defined. For the inner link, it is not clear what mass properties to use for the rigid tip body. One possible choice would be the combined elbow drive, outer link (rigidized) and tip payload, with the elbow joint locked at some arbitrary elbow angle. For the outer link, the natural choice is to use the actual tip payload as the equivalent tip body.

Given a particular set of assumed mode shapes $\phi_i^c(x)$ for each link, the generalized eigenvalue problem describing the small vibrations of the 2-D elastic arm around a given configuration is given as:

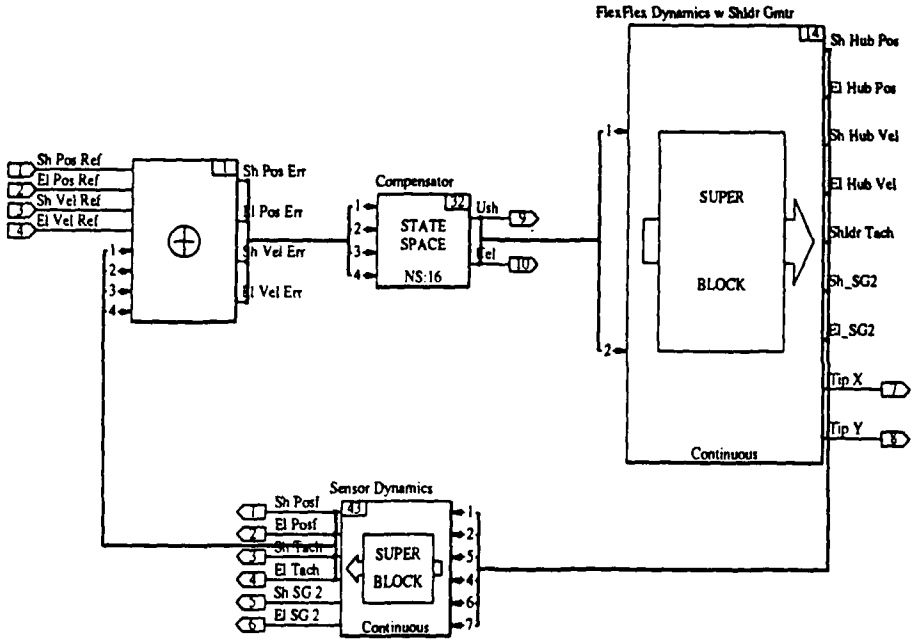

Figure 2-5: Simulation Block Diagram for the 2-D Nonlinear Elastic Dynamic Model

$$\left(\bar{M}(\theta_0^E)s^2 + Ds + K\right) X(s) = 0 \qquad (2-9)$$

where θ_0^E is the reference elbow joint angle.

For each particular choice of the assumed modes, one can derive the system vibration frequencies Ω^p and the system mode shapes $\Phi^p(x)$ by solving for (2-9). Detailed numerical studies have shown that accurate prediction of these frequencies and mode shapes is not sensitive to the particular choice of the mass properties of the equivalent rigid body for the inner link. Figure 2-6 shows transfer functions from shoulder motor torque to shoulder motor velocity for two cases. Three modes are used for each elastic link and the elbow joint is unlocked. The solid line results from computing the inner link mode shapes using the nominal equivalent rigid body payload mass properties m_p^S and $I_p^S(\theta_E = 0°)$; this corresponds to the maximum value for payload mass and inertia at the shoulder tip. For the dashed line of Fig. 2-6, the equivalent payload is chosen to include only the elbow actuator stator; compared to the nominal case, this represents a reduction of three in m_p^S and two orders of magnitude in I_p^S. Despite the gross differences in the mass properties chosen for the inner link payload, very little difference is seen between the two plots; the poles (system mode frequencies) and the zeroes of the transfer function remain essentially invariant. The system mode shapes (not shown here) are also essentially the same.

Finally, we consider the system modes for a future version of the experimental arm having a 12-ft reach, twice that of the current configuration. In this case, elastic links of the same bending stiffness are used, and their lengths chosen to give 6 feet between joint-

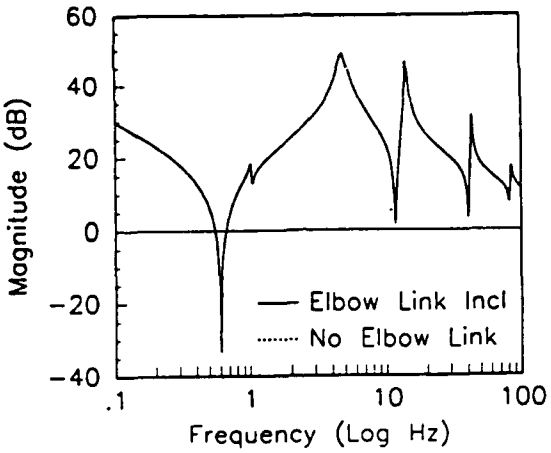

Figure 2-6: Open-loop transfer function from shoulder torque to shoulder angle obtained for two different tip body mass properties of the inner elastic link (6-ft arm in extended configuration)

axes. Figure 2-7a. shows the transfer function from shoulder motor torque to shoulder motor velocity, while Fig. 2-7b. is from shoulder joint torque to output from a strain gauge mounted midway along the shoulder link. As with Fig. 2-6, the solid lines are obtained using the nominal m_p^S and $I_p^S(\theta_E = 0°)$ while the dashed lines use mode shapes of the inner link based on the equivalent payload mass properties of the elbow actuator stator alone. As can be seen, again the system frequencies are insensitive to the particular choice of the mass properties of the equivalent rigid-body payload.

2.3.2 Experimental Validation of the Linearized Models

In [2] we discussed the identification of the dynamic model for a single elastic link. We now compare the experimental versus analytical transfer functions for the 2-DOF manipulator in the flex-flex configuration. Figure 2-8 shows the transfer functions from shoulder motor torque to shoulder motor velocity for two nominal values of the elbow angle θ_E. During the frequency response tests, the elbow joint is left unlocked. The nominal elbow angles are 0° and 90° for Figs. 2-8.a and 2-8.b, respectively. The analytical results are based on a linearization of the model about nominal elbow angle and with 3 modes retained for each link. The natural vibrations of the 2-DOF system are predicted by Eq. (2-9). For each value of θ_E, the theoretical model matches the first two poles and zeros quite well, and the only significant difference is seen in the third mode at approximately 85 Hz. Note that for the experimental results, the flexible modes appear much more damped than shown in the model. This apparent structural damping is largely due to the significant amount of viscous and coulomb damping in the gearmotor, and the relatively coarse resolution obtained in the measurements. For the model, structural damping was assumed to be approximately 1.5% in each of the modes.

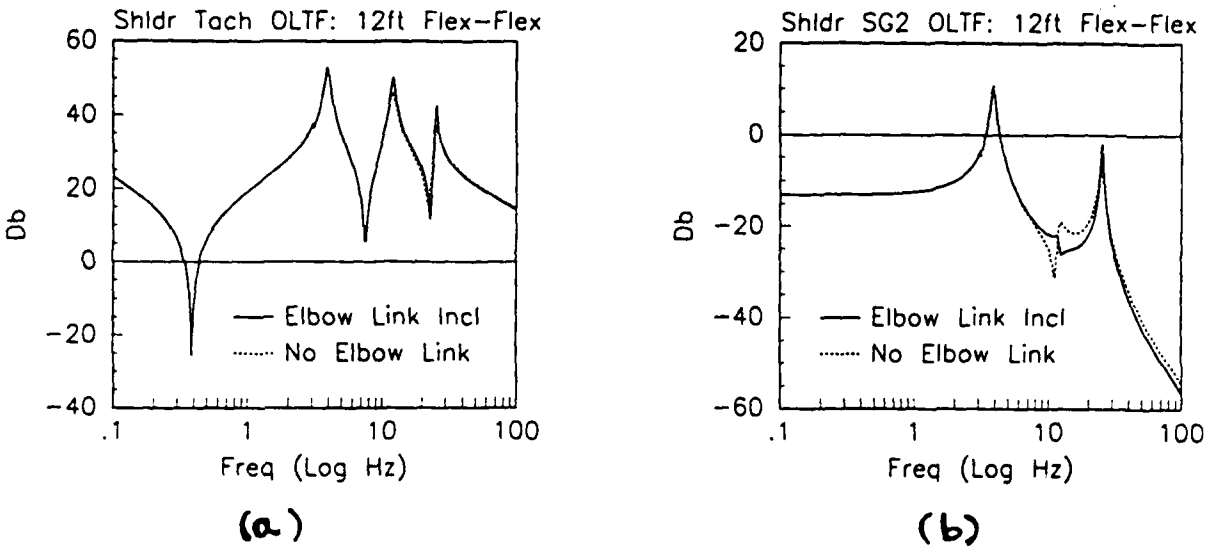

Figure 2-7: Open-loop transfer function (a) from shoulder torque to shoulder angle and (b) from shoulder torque to mid-span strain gauge obtained for two different tip body mass properties of the inner elastic link (12-ft arm in extended configuration)

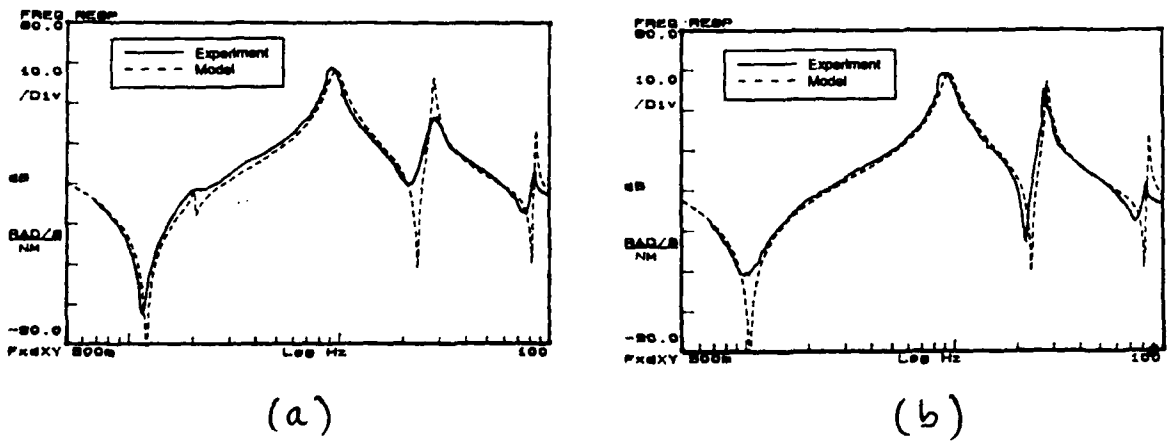

Figure 2-8: Experimental versus Analytical Transfer Function from Shoulder Motor Torque to Shoulder Motor Velocity for an elbow angle equal to (a) 0° and (b) 90°

Elbow Angle = 0°				
Index	Shldr Link (Hz)		Elbow Link (Hz)	
j	Ω_{1j}	ω_{1j}	Ω_{2j}	ω_{2j}
1	1.39	9.34	0.46	2.04
2	18.0	26.7	3.33	9.85
3	77.6	84.1	33.1	35.3
Elbow Angle = 90°				
Index	Shldr Link (Hz)		Elbow Link (Hz)	
j	Ω_{1j}	ω_{1j}	Ω_{2j}	ω_{2j}
1	1.19	9.32	0.53	2.00
2	17.9	26.7	2.90	9.83
3	77.3	84.1	33.0	35.3

Table 2.1: Analytical Clamped-Free (Ω_i) and Free-Free (ω_i) Frequencies for the 2-DOF arm with a large tip payload

Table 2.1 summarizes the free-free (i.e., both joints free) and clamped-free (i.e., both joints locked) frequencies of the flex-flex manipulator for elbow angles of 0° and 90°. As seen in the table, the free-free frequencies ω_i are insensitve to the elbow angle as the ω_i do not vary by more than 2%; however, the first bending frequencies Ω_1 vary as much as 15%.

2.3.3 Experimental Validation of the Nonlinear Dynamic Models

The nonlinear dynamic model is validated by comparing simulated and experimental time histories of given sensors for large angle motion of the structure. Figure 2-9 shows time histories of the experimental and simulated joint angles, velocities and strain-gauges output for a slew maneuver of the arm in the rigid-flex configuration [2]. Fifth-order splines are used as the joint angle reference commands for an independent joint Proportional and Derivative controller. The PD control commands are shaped with digital lowpass filters to provide gain stabilization of the higher modes. Note that here, the simplified dynamic model (for which the terms in the mass matrix and the nonlinear torques dependent on the elastic coordinates are deleted) is used in the simulation. Figure 2-10 shows time histories for a similar maneuver with the arm in a flex-flex configuration. The top two plots of Figure 2-10 show the joint angle responses for a 20° step command on each joint. These responses are dominated by the rigid body dynamics. To highlight the elastic dynamics, the bottom plot compares the experimental and simulated response of voltage output from a strain gauge sensor mounted at about mid-span on the elbow link. In each plot, good agreement is seen between model and experiment.

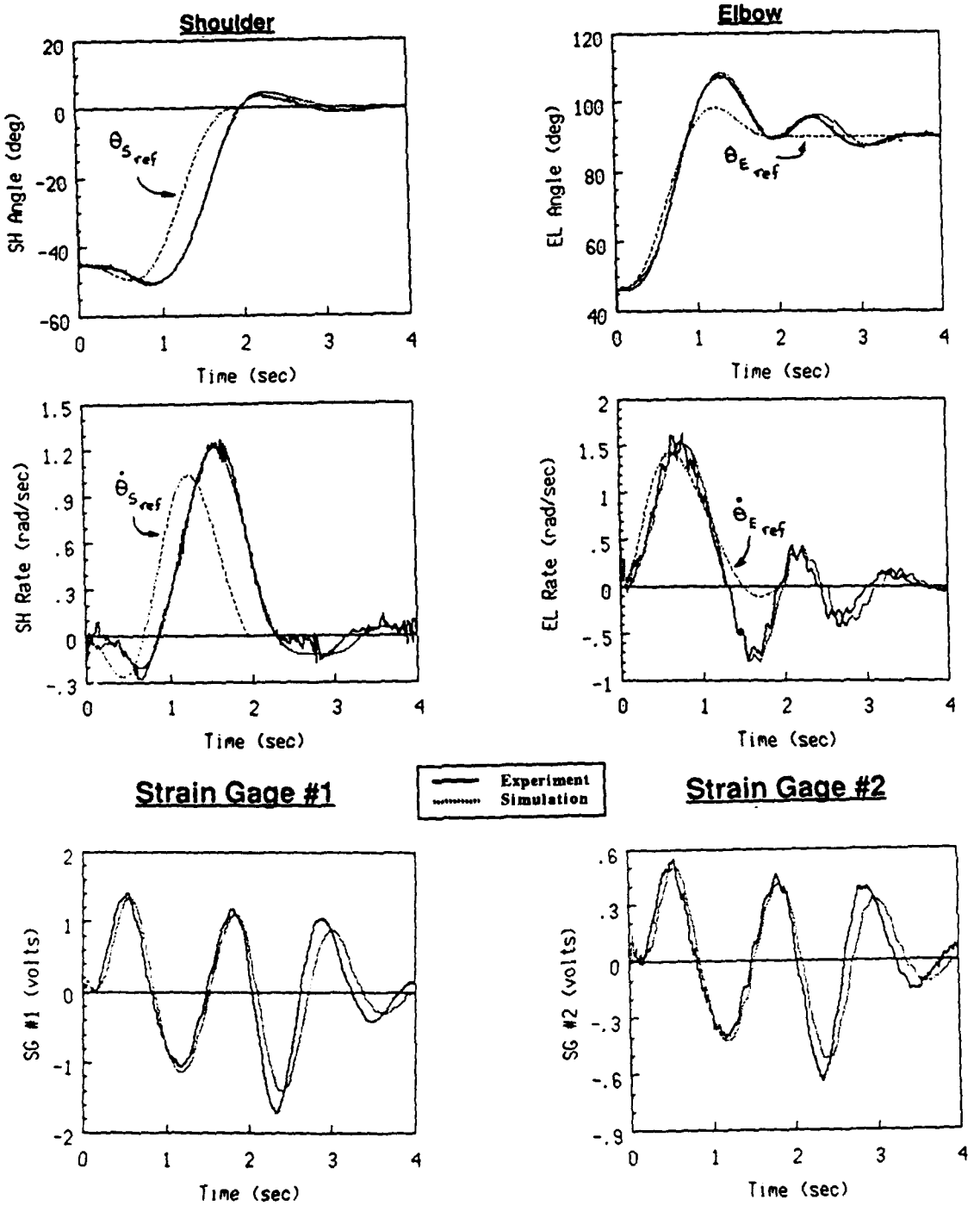

Figure 2-9: Experimental and Simulated Step Responses using PD Control for arm in rigid-flex configuration

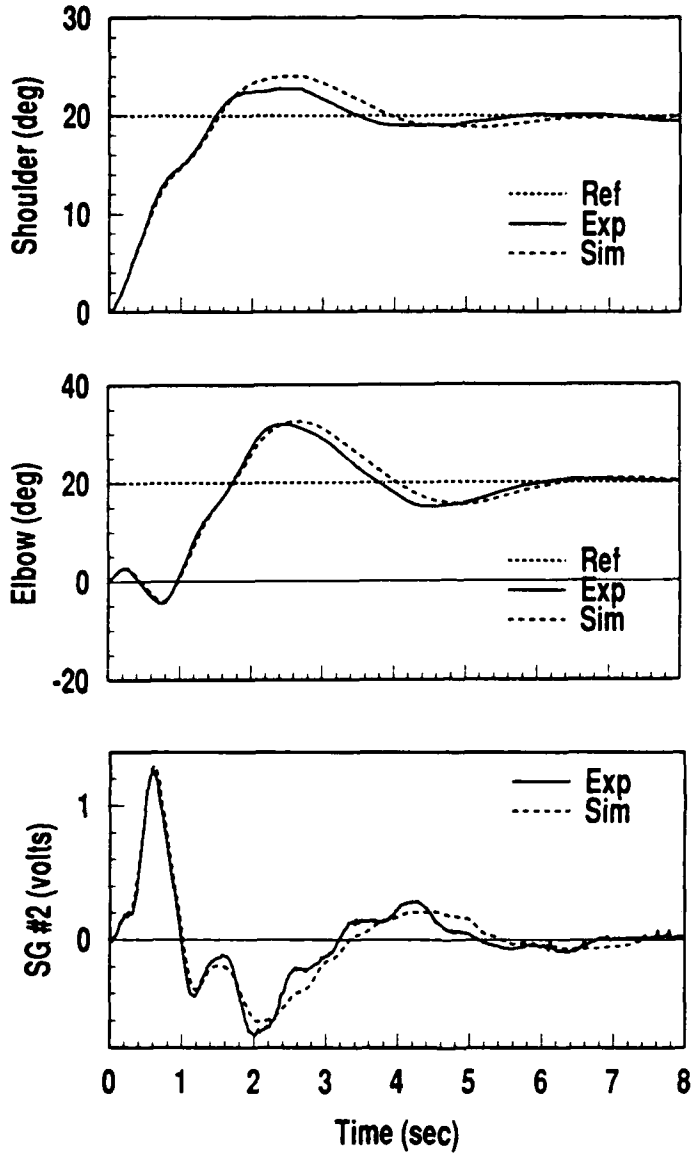

Figure 2-10: Experimental and Simulated Step Responses using PD Control for arm in flex-flex configuration

2.4 Conclusion

The derivation of analytical dynamic models for articulated elastic structures has been discussed. Kane's method allows for straightforward derivation of the equations of motion. The validation of the 2-D dynamic model has also been successfully obtained. From the tests performed so far on the experimental structure, it seems that the simplest dynamic model for which the first-order terms in the elastic coordinates are neglected in the mass matrix and nonlinear torque expressions accurately predicts the rigid/elastic coupling effects. Design and implementation of control designs for the 2-D structure are discussed in the next Chapter.

Chapter 3

Control Law Designs and Implementations

In this section, linear control designs based on the Linear Quadratic Gaussian with Loop Transfer Recovery (LQG/LTR) theory are discussed first for a single elastic link and then for the 2-DOF elastic arm in the rigid-flex and flex-flex configurations. Appendix C provides a partial listing of C-code subroutines used to implement (on the real-time control system) a sample control law for the 2DOF manipulator.

3.1 Single Link Active Modal Control

For these experiments, the outer elastic link of the manipulator is used with the elbow joint effectively grounded (by turning off air supply to the elbow air bearing). During the first phase of this contract [2], we demonstrated a high-performance LQG controller for the outer link configured with a small payload of mass $m_p = 1.4kg$. Below, we address the more challenging problem of designing a high-performance active modal controller for the case of a much larger payload ($m_p = 4.4kg$). While we have have designed and implemented several controllers using various sets sets of sensors, the best results were obtained with an LQG design using joint position and velocity sensors along with a strain gauge mounted to the link. After presenting this design and experimental results, we then examine the controller's sensitivity to changes in payload moment-of-inertia and one method we have used to yield a more robust compensator design.

Control Design Issues for Heavy Payloads

For large payloads, a high-performance controller is more difficult to achieve for two reasons. Foremost is the fact that the system's first cantilevered bending frequency Ω_c decreases with larger payloads. In our case, Ω_c decreases by a factor of two (from $1.2Hz$ to $0.6Hz$ for the small and large payloads, respectivley). When using a colocated control scheme, acceptably damped closed-loop position bandwidth has been shown to be fundamentally limited to $0.5\Omega_c$. For the small payload case, this fundamental limit was overcome with a LQG regulator and estimator design incorporating tip velocity measure-

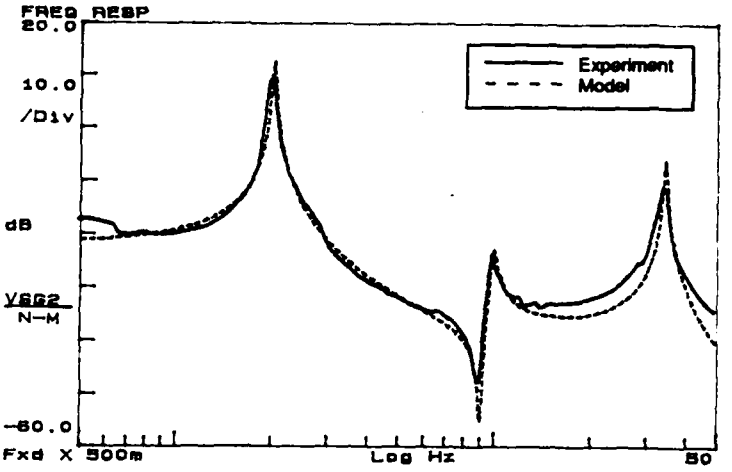

Figure 3-1: Experimental transfer function from elbow torque to voltage output of a strain guage mounted near the midpoint of the elbow link. Intended to primarily sense the first bending mode, the strain gauge was located near a strain anti-node of the first mode. As the frequency response illustrates, this results in a near pole-zero cancellation of the second mode and provides $35dB$ *attenuation compared to the first mode.*

ments. With this non-colocated controller, closed-loop bandwiths on the order of $0.9\Omega_c$ were achieved. However, as discussed in [2], increasingly large payloads effectively "pin" the tip. As a result, the elastic bending modes become *poorly observable* with a tip sensor, and thus, tip sensors are not effective for active modal damping of the dominant bending modes. To remedy this problem, we have made use of strain gauge sensors mounted along the link(s). As discussed in [2], the strain gauge location was optimized to maximize the observability of the dominant bending mode (see Fig. 3-1). The results presented below demonstrate the active modal damping improvements achieved with the use of strain sensors, but first we breifly review the LQG/LTR design method used.

3.1.1 LQG/LTR Controller Design Method

As noted above, the elbow joint is assumed grounded; thus, a separate model expressed in modal form (derived previously in [2]) is used for the outer elastic link. For the control design, only the first two flexible modes are retained, yielding a 6th-order state-space model. Using the Separation Theorem, the controller design is done in two steps: 1) design of a full-state feedback regulator, and 2) design of a steady-state estimator. The resulting compensator is then analyzed in terms of robustness for the resulting closed-loop system. When necessary, frequency-shaped weightings are used in the regulator's performance index to provide gain stabilization of the uncontrolled higher frequency modes. (Frequency shaping of the performance index is discussed later in section 3.3.)

Regulator Design

The regulator is designed to optimize a given quadratic performance index of the following form:

$$J_y = \int_{-\infty}^{+\infty} (y^t Q y + \rho u_e^2) dt \qquad (3-1)$$

where $y = C_y x$ is a vector of user-selected plant outputs, Q is a diagonal weighting matrix on y, and ρ is a weighting on the control torque u_e. The paramater ρ is used as a "tuning knob" to adjust the rigid-body bandwidth, based on the available peak torque from the actuator. The regulator closed-loop poles are the stable roots of the following characteristic equation:

$$det\left[\rho I + H^T(-s)QH(+s)\right] = 0 \qquad (3-2)$$

where H(s) is the transfer function matrix from $u(s)$ to $y(s)$. In order to help in the choice of outputs y and the diagonal matrix Q, we use a general property of the optimal regulator root-locus derived in [8]. When the control weighting ρ tends to zero, ("cheap control"), p of the regulator poles are obtained as the stable transmission zeros of the following system of order $2n$:

$$\begin{aligned} A_{aug} &= \begin{bmatrix} A & 0 \\ C_y^T Q C_y & -A^T \end{bmatrix} \\ B_{aug}^T &= \begin{bmatrix} B^T & 0 \end{bmatrix} \\ C_{aug} &= \begin{bmatrix} 0 & -B^T \end{bmatrix} \end{aligned} \qquad (3\text{-}3)$$

where A and B are the state-space and control distibution matrices, respectively. Studying the location of these finite zeros for a given J_y will guide the designer in choosing the set of outputs y and the elements of the Q matrix.

Figure 3-2 shows the optimal regulator root locus as ρ is varied. [1] In this figure, the open loop poles are marked by x's, while the asymptotic regulator pole locations (for $\rho = 0$) are marked by circles. In this design for the large payload, the outputs of y were initially chosen to be the joint angle and joint velocity. In this case, the finite zeros on the $j\omega$ axis would correspond to the the open-loop transmission zeros of the system (A, B, C_y) (i.e., the cantilevered bending frequencies of the arm). For the chosen form of the system model, the measurement vector C_y is a function of the modal slopes at the hub; by directly weighting the modal slopes of C_y corresponding to the first two

[1] see Appendix C for a listing of the user-defined MATRIXx functions developed to generate the optimal regulator and estimator root-loci shown in this chapter.

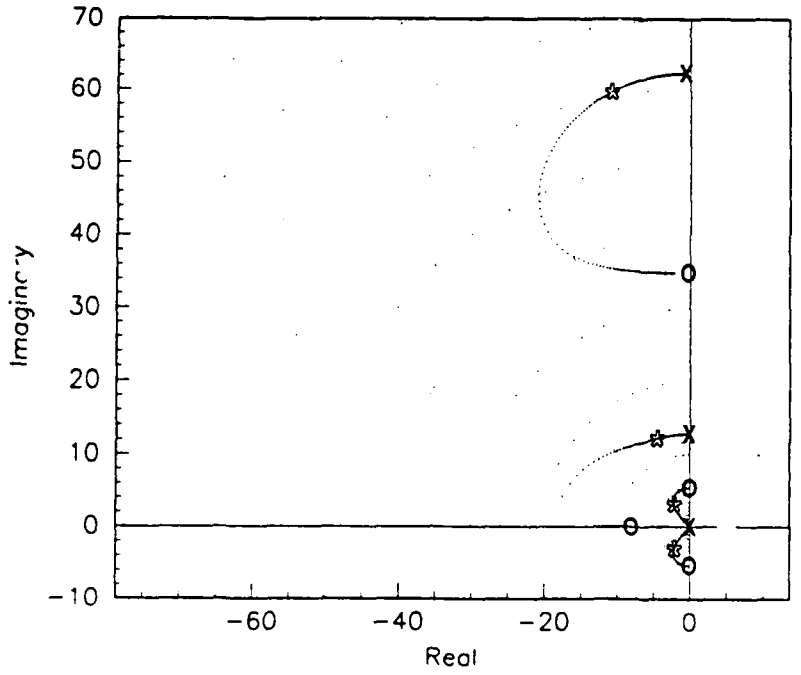

Figure 3-2: Optimal regulator root locus versus control weighting ρ for LQR design of outer elastic link with a large payload.

elastic modes, the finite zeros are shifted upward to the more desirable locations shown in Fig. 3-2. The chosen closed-loop regulator poles are marked in the figure by a star. For this value of ρ, all of the modes are well-damped, and the rigid-body poles give a bandwidth roughly equal to $0.85\Omega_c$.

Estimator Design

The Loop Transfer Recovery method applied here in its simplest form [7] is used to select the process noise intensity q (modelled here as actuator noise) for the estimator design. Central to this method is the proper choice of the ratios $r_i = \frac{R_{prim}}{R_{aux_i}}$, where R_{prim} is the noise intensity for the "primary" sensor (i.e., the joint angle in our case) and R_{aux_i} is the noise intensity for the "auxiliary" sensors (i.e., the joint rate and strain gauge sensor). The parameters r_i are selected to adjust the relative "participation" of the sensors in the feedback loop. When the process noise intensity q tends to infinity, p of the estimator poles will asymptotically converge towards *finite* locations which are functions of r_i. For $r_i = 0$, the finite estimator poles will be the transmission zeros of the "primary" sensor. For $r_i = \infty$, the finite poles will be the transmission zeros of the "auxiliary" sensors. The final values of r_i are then chosen so that the finite poles are at some intermediate location between these two sets of zeros. Note that by using the duality between estimator and regulator design, these zeros can be obtained as the transmission zeros of a system of order $2n$ similar to Eq. (3-3). Also, when the "auxiliary" sensor is a rate sensor, r_i is

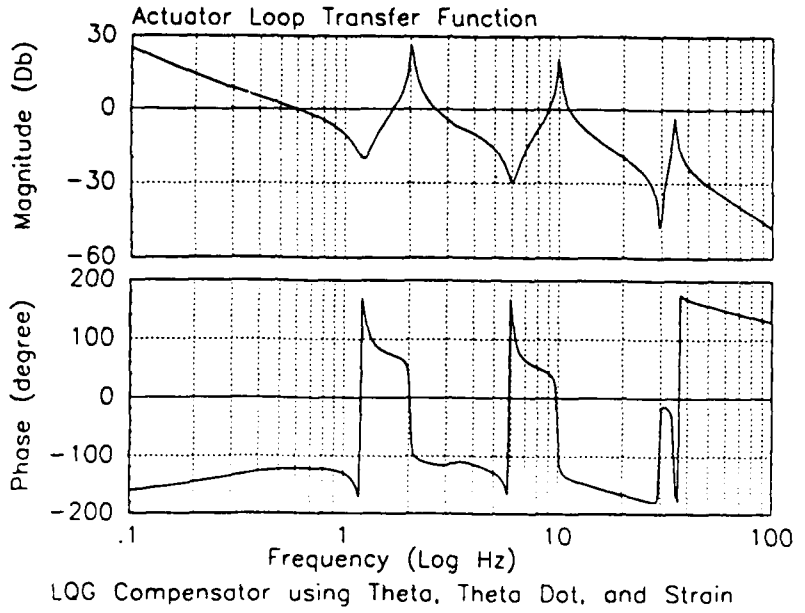

Figure 3-3: Actuator loop transfer function for an LQG/LTR compensator designed for outer elastic link with the large payload.

chosen based on obtaining "reasonnable" values for the DC gains of the resulting position and rate compensators (typically, a classically designed, low-bandwidth PD compensator is used as a baseline; "reasonnable" values of these gains will correspond to an increase by a factor of 3 to 10). Having chosen r_i, the process noise intensity q is adjusted to recover the actuator loop shape given by the set of regulator gains.

Using this method, an estimator has been designed for the large payload case using the joint angle and velocity sensors, and a strain gauge sensor located near the midpoint of the outer elastic link. In each case, a continuous s-plane design was done to select the regulator and estimator gains. Using the resulting continuous compensator, Fig. 3-3 shows the actuator loop transfer function. In this figure, a 1st-order Pade approximation was included to model a $15ms$ sampling delay. As can be seen, the third mode (uncontrolled) is gain stabilized such that frequency shaping of the regulator performance index is not required.

3.1.2 Experimental Results

For digital implementation on the experimental testbed, a discrete compensator is obtained by applying a bi-linear Tustin transformation to the continous compensator. For the experiments here, a $15ms$ sampling period was used.

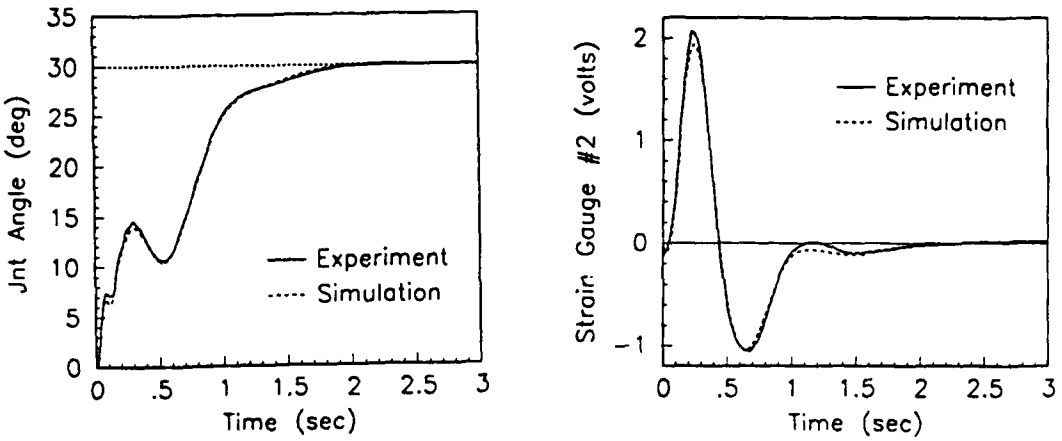

Figure 3-4: Experimental and simulated closed-loop step responses using an LQG controller for the outer elastic link with the large payload.

Figure 3-4 shows the experiment and simulated step responses using the discretized LQG/LTR compensator. Excellent agreement is seen between the experiment and simulation. For performance comparison, a simple proportional and derivative (PD) controller has also been designed; a first-order low pass filter is added in series with the PD controller in order to gain stabilize the unmodelled high-frequency modes. Fig. 3-5 shows a step response for the baseline controller. Comparing the joint angle traces, the LQG controller yields a factor of two improvement in rise and settling times, and with no overshoot or steady-state offset. To compare the active modal damping of these two controllers to an external disturbance, Fig. 3-6 shows open-loop and closed-loop responses to a sinusoidal force applied midway along the elastic link. Here, the output from a strain gauge is recorded from the time the disturbance is turned off. As can be seen, the LQG/LTR controller significantly increases the closed-loop damping of the dominant vibration mode by roughly a factor of 2.5.

3.1.3 Parameter Robust LQG/LTR Design

In this section, we analyze the closed-loop sensitivity of the LQG/LTR controller discussed above to parameter variations from the nominal plant. Demonstrating the closed-loop sensitivity to these changes, we then discuss a method that has been used to "robustify" the compensator design. Using this method, simulation results demonstrate the robustness improvements achieved.

For the outer elastic link, the payload's moment-of-inertia (MOI) can be adjusted

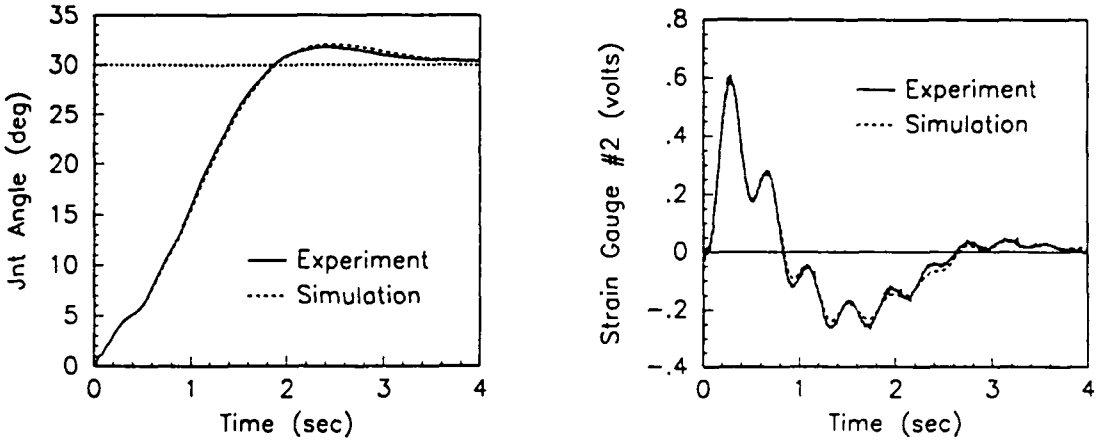

Figure 3-5: Experimental and simulated closed-loop step responses using a PD controller for the outer elastic link with the large payload.

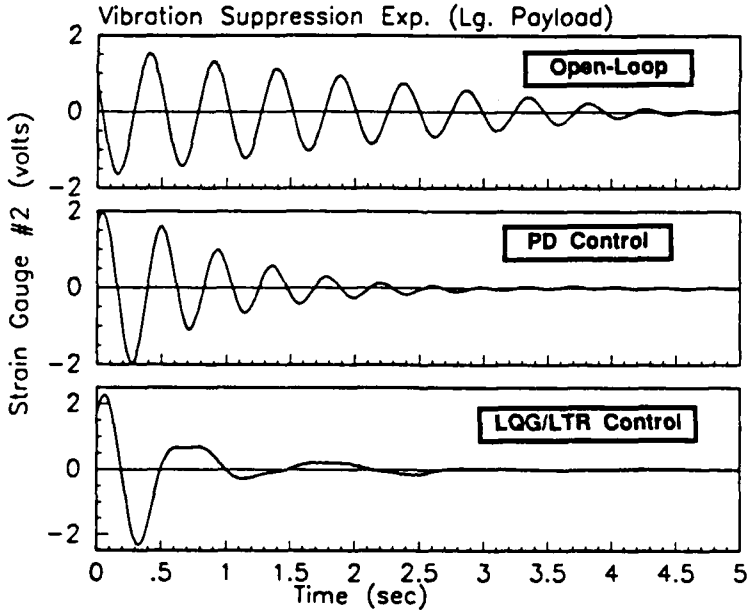

Figure 3-6: Experimental open-loop and closed-loop responses to a disturbance force applied along the elastic link.

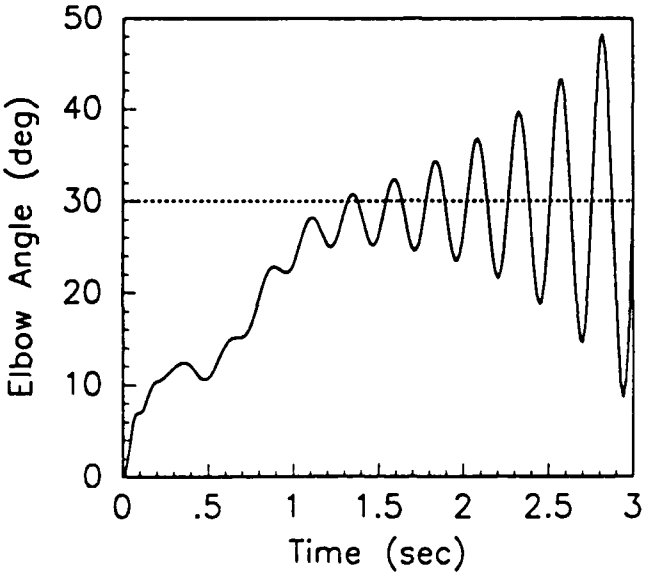

Figure 3-7: Simulated closed-loop step response using the nominal LQG/LTR compensator for the outer link with a reduced payload moment-of-inertia.

whereby the first resonant (free-free) frequency of the outer link ranges from $2.0Hz$ to $4.0Hz$. The LQG/LTR controller discussed above was designed for the nominal case of the maximum payload MOI $I_p^{max} = 0.32kg - m^2$. To demonstrate the controller's sensitivity to a reduction in payload inertia, Fig. 3-7 shows the unstable step response for a payload MOI of $I_p' = 0.4I_p^{max}$. For this payload configuration, the first resonant frequency increases to $3.0Hz$, compared to $2.0Hz$ in the nominal plant. While this represents a significant change from the nominal plant, instability actually occurs for smaller reductions in I_p (on the order of $0.2I_p^{max}$).

The Parameter Robust LQG/LTR method is based on a numerical re-optimization of the nominal compensator design to handle several open-loop plant models including the nominal model and ones corresponding to the worst case combination(s) of modal parameter variations. Developed by Professor Uy-Loi LY, the software program SANDY [?] is used for doing the numerical reoptimization. The algorithm minimizes a weighted sum of n performance indices:

$$J = \sum_{i=1}^{n} \omega_i J_i \qquad (3-4)$$

where each index J_i is the expected value of the steady-state quadratic performance index evaluated for a given open-loop model obtained for a given set of open-loop parameters. The general expression for J_i is

$$J_i = \lim_{t_f \to \infty} \frac{1}{t_f} E \int_0^{t_f} (y^t Q y + u^t R u) dt \qquad (3-5)$$

where the expected value $E[\cdot]$ is taken over the ensemble of random noise disturbances applied at the plant input u (process noise) and at the plant outputs y (measurement

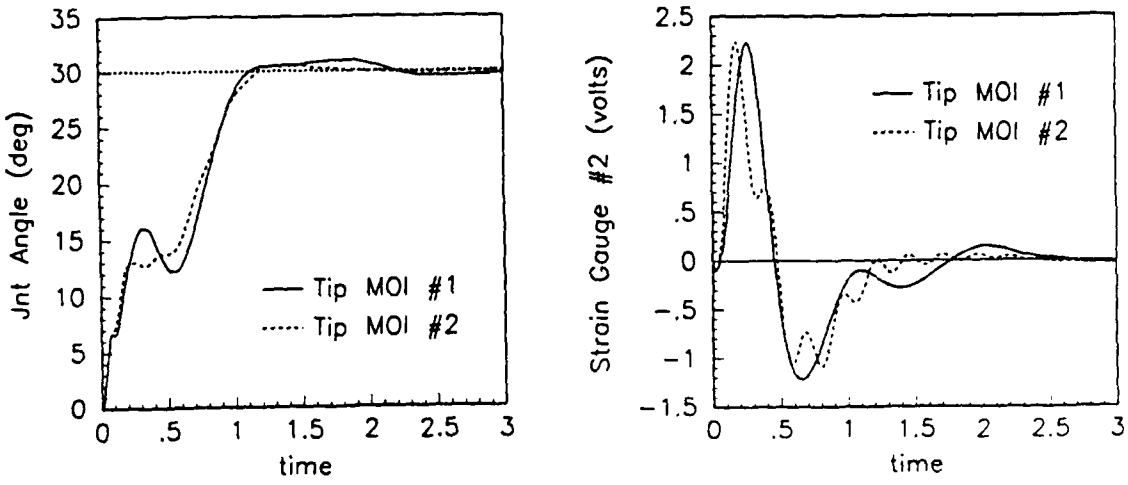

Figure 3-8: Simulated closed-loop step responses using the Paramter Robust LQG/LTR compensator for two payload MOI configurations: Tip MOI #1 = I_p^{max}, and MOI #2 = $0.4I_p^{max}$.

noise). The analog compensator, whose coefficients are to be optimized by the code, is given as:

$$\begin{aligned} \dot{z} &= A_c z + B_c y \\ u &= C_c z \end{aligned} \tag{3-6}$$

where the controller matrices (A_c, B_c, C_c) form a *minimal realization* [9]. The performance index and its gradients with respect to the compensator gains are evaluated analytically. A gradient search method (developed by Gill and Murray) based on a modified quasi-Newton algorithm is used for the numerical minimization of J. The algorithm will then find the elements of A_c, B_c, and C_c, given an initial guess (e.g., the nominal controller). The resulting compensator will be stable for each open-loop model included in the set $[1, \cdots, n]$ and is therefore expected to be robust to parameter changes.

To illustrate the method, we consider the range of payload inertias from I_p^{max} to I_p'. Using the performance indices specified for the two open-loop models corresponding to I_p^{max} and I_p', a single compensator was obtained. Figure 3-8 shows the simulated step responses for the two payload configurations. Despite the significant plant parameter variations, the SANDY compensator performs well for both cases.

3.2 Rigid-Flex Control

For these experiments, the arm is in the rigid-flex configuration. A feedback controller has been designed to perform a large angle slew maneuver of the arm in an extended configuration. The coupled 2-DOF arm dynamics are linearized for an elbow angle of 0° (arm extended). The method of successive loop closures is used for the controller design. Using the same performance index and sensor inputs as discussed above, an LQG/LTR controller is designed for the elbow link (with the shoulder loop open). A simple PD controller is then designed for the shoulder link (with the elbow loop closed). A second-order lag filter is added in series with the PD controller in order to prevent excitation of the unmodelled high-frequency dynamics.

A fifth-order spline polynomial of time is used to generate the shoulder angle profile while the elbow joint angle is commanded to stay at 0°. To improve the trajectory tracking, a feedforward torque command is also used. The feedforward torques are computed assuming that the manipulator has rigid links:

$$\begin{bmatrix} T_s^c \\ T_e^c \end{bmatrix} = M_{RR}(\theta_e^c) \begin{bmatrix} \ddot{\theta}_s^c \\ 0 \end{bmatrix} \tag{3-7}$$

where $M_{RR}(\theta_e^c)$ is the 2×2 mass matrix of the equivalent rigid manipulator.

Experimental time histories of the joint angles are shown in Fig. 3-9 for 2 control laws, (1) two independent PD controllers for the shoulder and elbow actuators with shaping filters for gain stabilization of the high frequency modes and (2) the feedback/feedforward controller discussed above. As seen from the experimental time histories, the second controller with the feedforward torque commands reduces by a factor of three the peak elbow angle excursion during the slew maneuver for the first controller.

3.3 Flex-Flex Control

In this section, we primarily focus on the design of a full-state feedback controller for the arm in the flex-flex configuration with the large payload [3]. In order to achieve high-bandwidth position control, the analysis will show the importance of incorporating tip position outputs into the regulator performance index. Not surprisingly, the same will be shown true for the estimator design as well. Unfortunately, the experimental testbed has yet to be instrumented with a tip position sensor. As such, the controller designs presented will be evaluated by simulation using the nonlinear dynamic model discussed in the previous chapter.

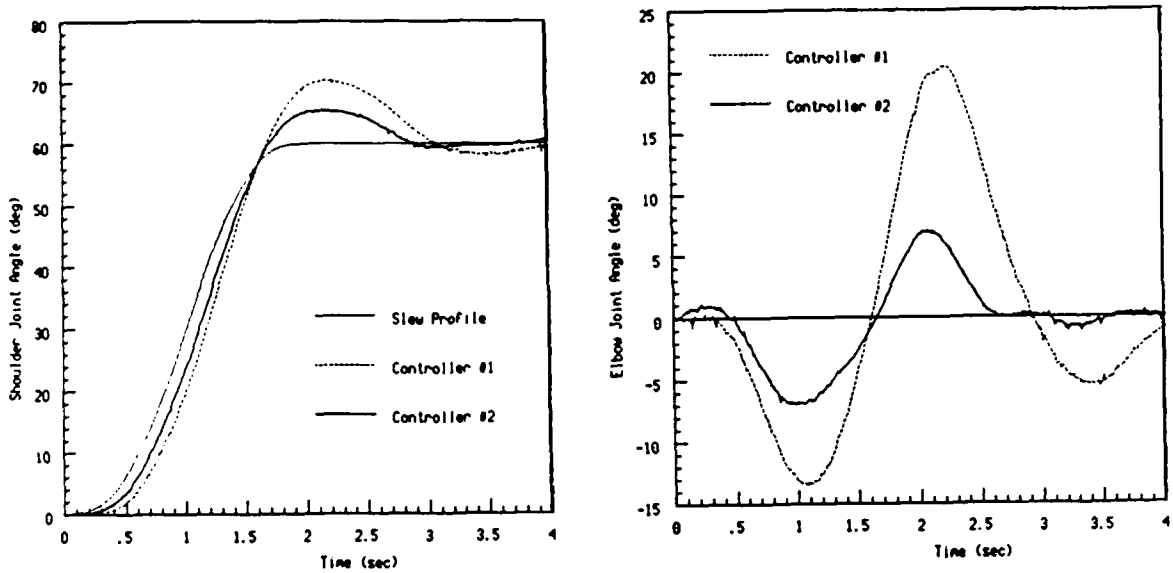

Figure 3-9: Comparison of two controllers for a large angle slew maneuver of the rigid/elastic planar structure. The shoulder angle command is a fifth-order spline function of time. The elbow angle is commanded to be zero (extended arm configuration).

3.3.1 Regulator Designs

A constant gains linear quadratic regulator (LQR) is designed for the open-loop system (A, B, C) obtained by linearizing the nonlinear dynamic equations (2-2) for a given arm configuration. Here, we have arbitrarily chosen the configuration for $\theta_e = 45°$. The output vector defined by the C matrix includes the joint angles, joint rates, strain gauges located on each link, and tip position and velocity coordinates.

The design goal is to achieve a closed-loop bandwidth for the rigid-body poles at least equal to the lowest fundamental vibration frequency Ω_c of the arm with its joints locked (0.5 Hz for the arm configuration chosen here). The closed-loop damping should be at least 50% for the rigid-body poles and 30% for the dominant elastic modes.

Similar to that used for the single link, the general form of the quadratic performance index (P.I.)for the 2-DOF case used here is:

$$J_y = \int_0^\infty \left[y^t Q y + \rho(u_s^2 + \rho_{se}^2 u_e^2) \right] dt \qquad (3-8)$$

where Q is a diagonal weighting matrix, $y = C_y x$ is a user-selected set of outputs, u_s and u_e are respectively the shoulder and elbow torques. The relative elbow to shoulder actuator weighting ρ_{se} is chosen as the ratio of the peak shoulder to peak elbow actuator torques.

To guide in selecting the regulated outputs of y and the elements of Q, we again make use of the optimal regulator root-loci and the location of their finite zeros for a given J_y. If the outputs of y consist of only the joint angles and joint rates, the finite zeroes (on the imaginary axis) correspond to the open-loop vibration frequencies of the arm with its joints locked. This is illustrated in the optimal root-locus shown in Fig. 3-10.a. In this figure, the poles for a nominal design value of ρ are marked by a shaded star. The slowest rigid-body poles with an acceptable damping coefficient will have a bandwidth equal to $0.5\Omega_c$ at most, and the closed-loop damping of the dominant elastic mode is about 25%.

When the outputs of y used in the P.I. include only tip position and velocity errors, the design goal is satisfied for the rigid-body poles but the closed-loop damping achieved for the elastic mode is less than 10%. As shown in Fig. 3-10.b one pair of the finite zeroes is lightly damped and nearly cancel the dominant free-free mode of the arm (2 Hz). This near pole-zero cancellation will always occur for the dominant elastic mode in the case of large tip payload-to-arm mass ratio because in this vibration mode, the arm is nearly pinned at the tip.

When the output vector y includes the tip position errors, joint rates and strain gauge errors, the corresponding set of finite zeroes (see Fig. 3-10.c) will attract the dominant closed-loop poles to acceptable locations. For the nominal value of ρ shown, the corresponding rigid-body bandwidth is now equal to $1.4\Omega_c$ and the closed-loop damping for the dominant elastic modes is equal to 30 %.

Once the best combination of sensors to include in the performance index has been chosen, frequency shaped weightings are used in the performance index to provide gain stabilization of the high-frequency unmodelled modes. To simplify the discussion, we return to the case of the performance index for the single link system with one torque input u_e. To incorporate frequency shaped weightings, Eq. 3-1 becomes:

$$J_f = \int_{-\infty}^{+\infty} \left[y^{*t} Q(j\omega) y + u_e^{*t} R(j\omega) u_e \right] d\omega \qquad (3-9)$$

where $Q(j\omega)$ and $R(j\omega)$ are frequency dependent weightings. (For our designs, $Q(j\omega)$ remains a diagonal matrix of constant gains.) If the control weighting $F(s = j\omega)$ is chosen as a lag filter:

$$R(s) = \rho \left| \frac{\beta s + 1}{\alpha s + 1} \right|^2 \qquad (3-10)$$

with $\beta > \alpha$, the resulting full-state feedback law will be of the form, [6]:

$$u_e(s) = -\frac{\alpha s + 1}{\beta' s + 1} K x(s) \qquad (3-11)$$

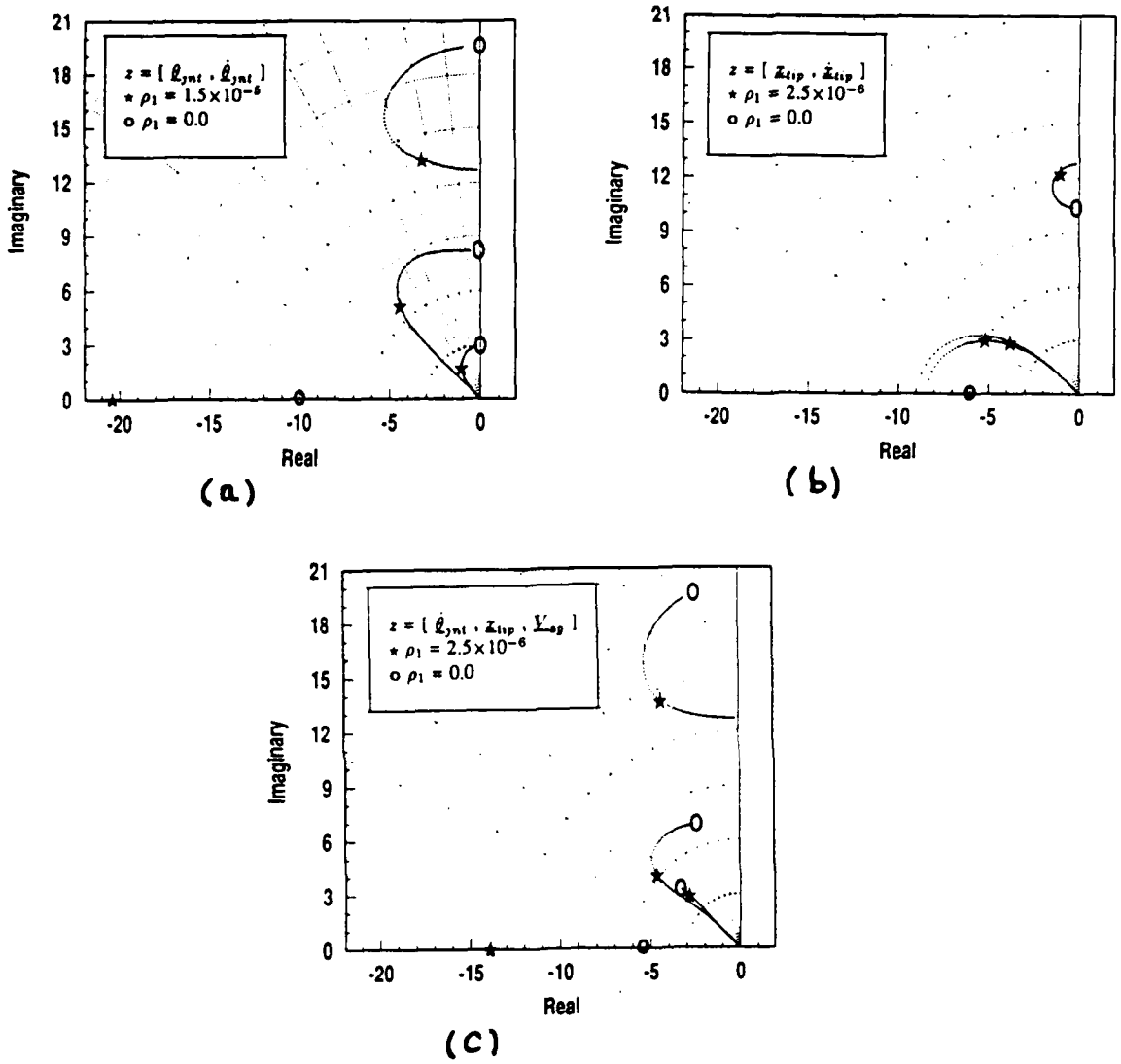

Figure 3-10: Optimal Regulator Root-Loci obtained for three different choices of the regulated outputs. Only the dominant closed-loop regulator poles obtained as a function of ρ_1 are shown here.

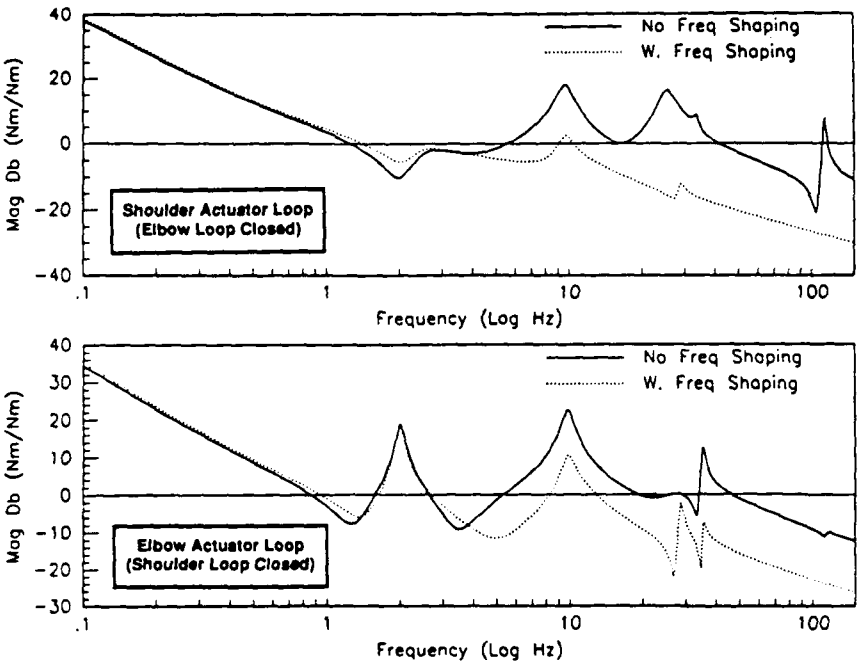

Figure 3-11: Magnitude plots of the shoulder and elbow actuator loop transfer functions demonstrating the effect of including frequency shaped weightings in the LQR performance index.

where K' is the row-vector of state-feedback gains and $-\frac{1}{\beta'}$ is the closed-loop location for the lag filter pole. The resulting actuator loop transfer function will have increased roll-off at high frequency. The proper choice of the lag filter coefficients will result in gain stabilization of the high-frequency modes. As before, parameter ρ is used as a "tuning knob" to adjust the rigid-body bandwidth, based on the available peak torque from the actuator.

Extending the method to the flex-flex case, Fig. 3-11 demonstrates the frequency shaping of the shoulder and elbow actuator loops. Using the nominal full-state feedback gains corresponding to Fig. 3-10.c, the solid lines in Fig. 3-11 are for the case without frequency shaping. Applying frequency-shaped weightings results in the dashed lines of Fig. 3-11 in which all modes above $10Hz$ gain stabilized.

In order to compare the best regulator design (i.e., the one which regulates tip position, joint velocity, and strain gauge errors) to the simple PD controller discussed in the previous chapter (see section 2.3.3), detailed closed-loop simulation was performed with the nonlinear dynamic model. The arm's joint position and rate commands are chosen as a fifth-order spline profile such that the tip follows a straight line in cartesian space for an equivalent rigid manipulator. The initial and final points of the tip trajectory correspond to $\theta_s = [-20°, +20°]$ and $\theta_e = [+60°, +30°]$ (recall that the control design was done for a linearization about $\theta_e = 45°$). Specified to reach the final position in 3

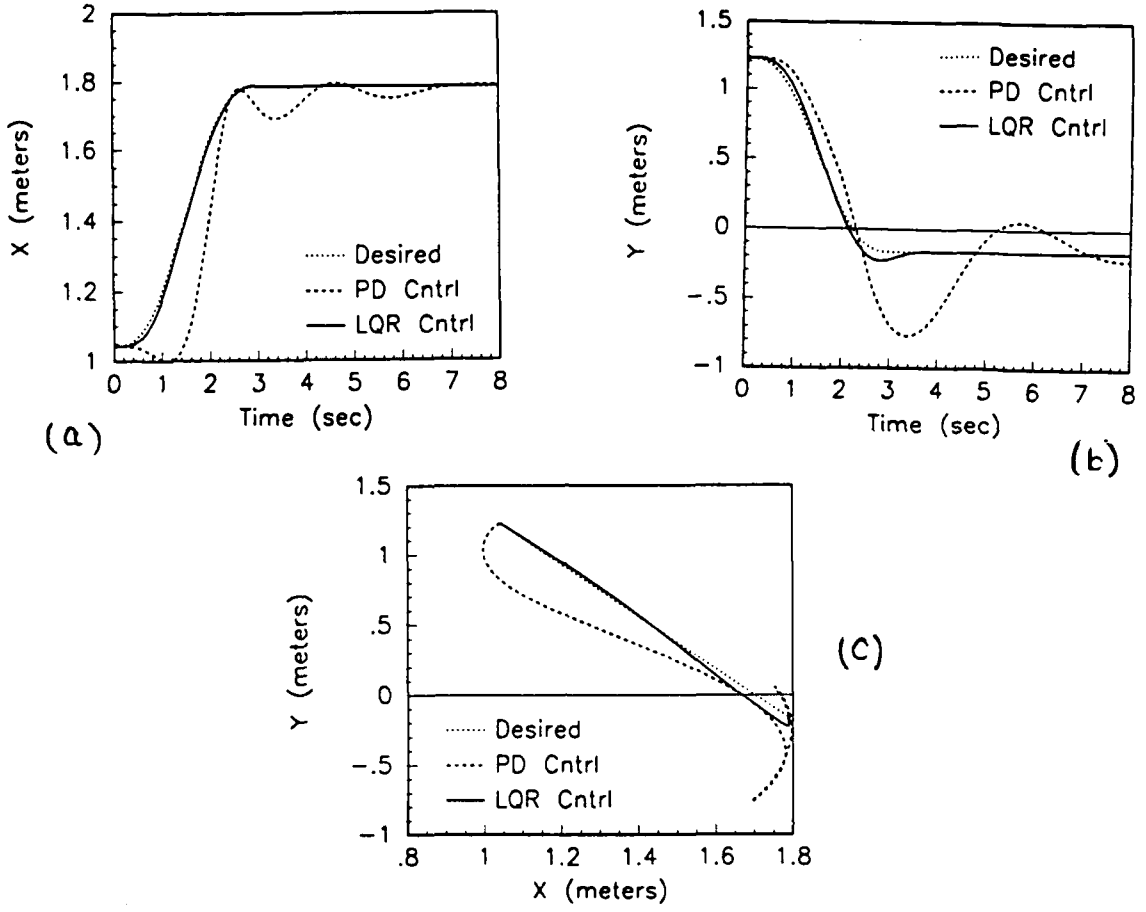

Figure 3-12: Simulated tip reponses for a constant gain regulator design and an independent PD controller.

seconds, the trajectory's maximimum tip velocity is 0.5 meters/second. The time traces of Fig. 3-12.(a,b) show the actual versus commanded tip trajectories obtained for the two controllers. while Fig. 3-12.c shows these results plotted in Cartesian space (i.e., a "birds-eye" view). The full-state feedback controller maintains good tracking along the trajectory, with just a small amount of overshoot. Under PD control, the tip undergoes large excursions from the desired straight-line path and exhibits excessive overshoot. Clearly, the full-state feedback controller—regulating a combination of tip position errors, joint rates, and bending strain—outperforms the colocated PD controller. But of course, the LQR cannot be implemented without a state estimator, which is addressed next.

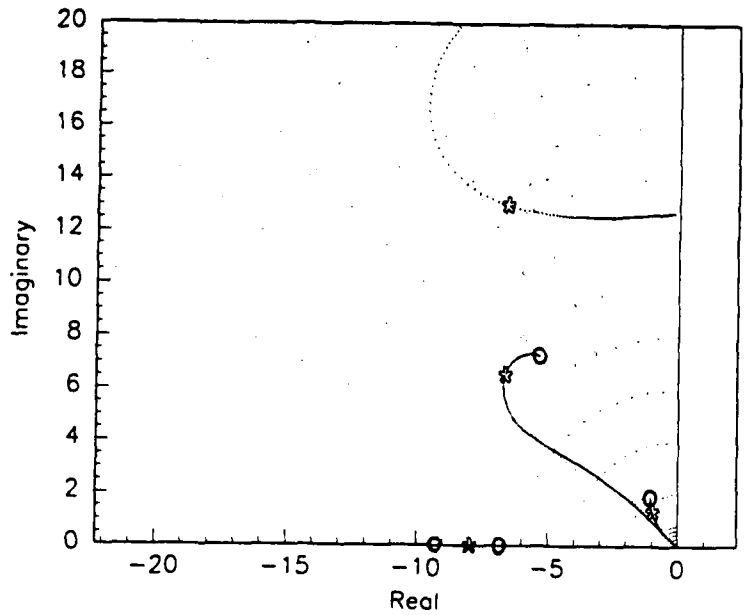

Figure 3-13: Optimal Estimator Root-Locus obtained using joint position, joint velocity, and strain gauge sensors for the flex-flex manipulator with a large payload.

3.3.2 Estimator Designs

For the regulator design, the closed-loop rigid-body bandwidth requirements were achieved by including tip position as a regulated output. Following a similar analysis for the estimator design, it can be shown that an end-point sensor is needed to meet requirements on the estimator's closed-loop rigid-body poles. Not having an end-point position sensor available, an initial estimator has been designed using the joint sensors and strain gauges. To demonstrate the limitations of such a design, we make use of the optimal estimator root-locus (the dual to the optimal regulator root-locus). Figure 3-13 shows the symmetric locus of closed-loop estimator poles versus the process noise intensity q. Similar to the regulator case, the circles designate the finite estimator pole locations, and the shaded stars mark the selected estimator eigenvalues for a nominal value of q. While acceptable damping is acheived for the dominant flex mode, the slowest rigid-body pole (corresponding to the elbow) is limited to a bandwidth of $0.5\Omega_c$. Nonetheless, a compensator was obtained by combining estimator with the regulator gains used in the full-state feedback controller above.

To see the effect of this less-than-desireable estimator design, Figure 3-14 shows the simulated closed-loop tip response using the same tip trajectory specified before. Comparing these plots to Fig. 3-12, while the LQG/LTR compensator exhibits slightly less tracking error and overshoot than the PD controller, it is quite evident that the performance achieved with the LQR is severely degraded by the poor estimator design.

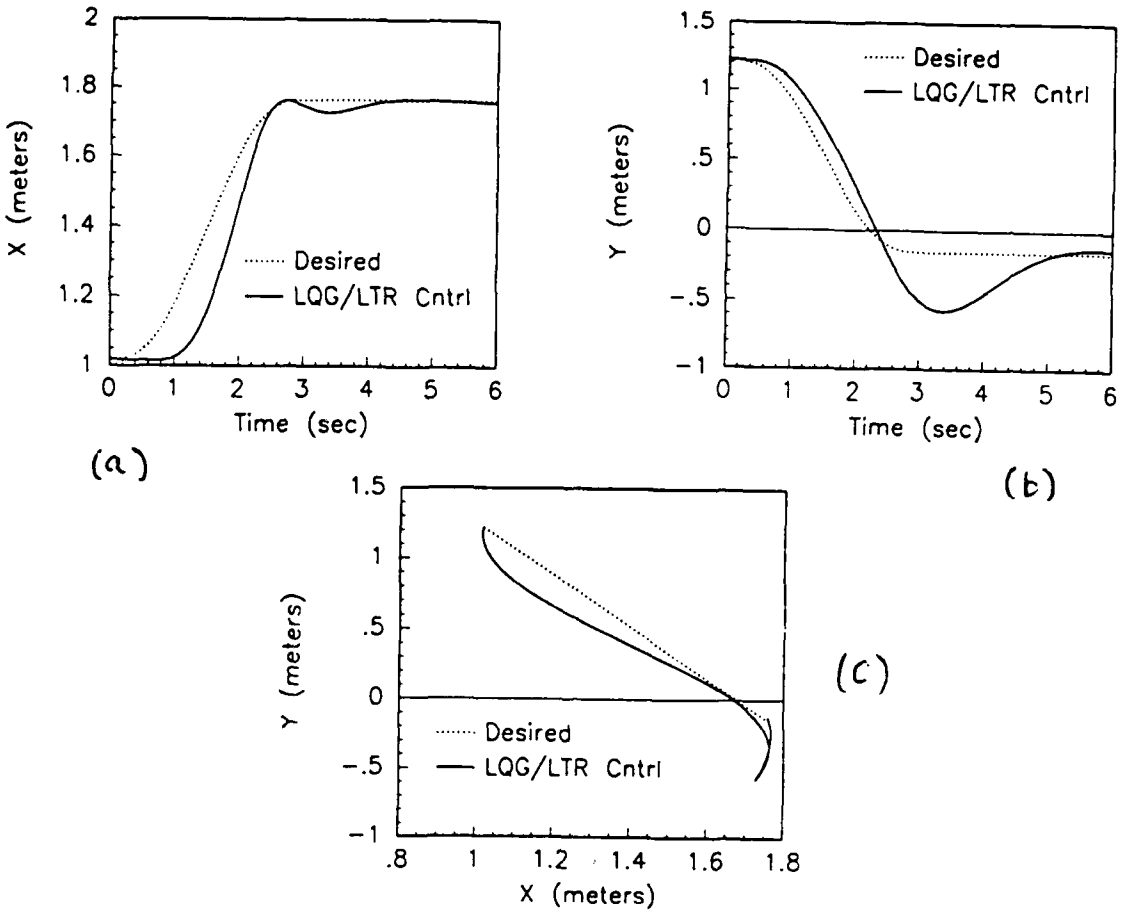

Figure 3-14: Simulated tip responses for the LQG/LTR compensator.

Once the experimental manipulator is instrumented with an end-point position sensor, future work will focus on the implementation of estimator designs incorporating tip sensing.

Thus far, we have limited our discussion to linear estimators. We will also begin to investigate the potential benefits of nonlinear estimator designs, such as a constant-gains extended Kalman Filter [10]. With this method, instead of updating the state estimate with a linear transition matrix, the time update is obtained by integrating the nonlinear equations of motion over the sample period. In this manner, the estimator accounts for the nonlinear dynamics of the manipulator, and potentially allows one set of regulator and estimator gains to achieve high performance over the entire workspace.

3.4 Conclusions

In this chapter, we have investigated various linear LQG-based controllers for three configurations of the experimental manipulator. Throughout, we have focused the controller designs for the manipulation of heavy payloads. For the single link case, we have demonstrated a method for improving compensator robustness to changes in plant parameters while maintaining a high degree of closed-loop performance. The robustification method can be readily extended to the multi-DOF problem. In the rigid-flex case, the use of feed-foward torques based on the rigid mass matrix was shown to improve command tracking. The idea can be applied to the flex-flex case as well. Finally, we have studied in depth the issues concerning regulator and estimator designs for the flex-flex case, showing the importance of using a combination of colocated rate sensors, noncolocated position sensors, and bending strain sensors.

References

[1] E. Schmitz, " Modeling and Control of a Planar Manipulator with an Elastic Forearm", *Proceedings of the 1989 IEEE Robotics and Automation Conference*, May 1989, pp. 894-899.

[2] E. Schmitz and M. F. Ramey, "Large Space Manipulators Study", First Annual Report to AFOSR, Contract F49620-88-C-0037, Martin Marietta Space Systems Company, July 1989.

[3] M.F. Ramey and E. Schmitz, "LQR Design for an Experimental Planar Elastic Arm with A Large Tip Payload", *Proceedings of the 1990 American Control Conference*, May 1990, pp. 1729-1732.

[4] C. M. Oakley and R. H. Cannon, Jr., "End-Point Control of a Two-Link Manipulator with a Very Flexible Forearm: Issues and Experiments", *Proceedings of the 1989 American Control Conference*, Pittsburgh, PA, June 1988

[5] C. E. Padilla and A. H. Von Flotow, "Nonlinear Strain-Displacement Relations in the Dynamics of a Two-Link Flexible Manipulator", Space Systems Laboratory Report # 6-89, Dept. of Aeronautics and Astronautics, MIT.

[6] B.D.O. Anderson and D.L. Mingori, "Use of Frequency Dependence in Linear Quadratic Control Problems to Frequency-Shape Robustness", Journal of Guidance, Control, and Dynamics, Vol.6, No.3, May-June 1985.

[7] J.C. Doyle, "Robustness with Observers", IEEE Transactions on Automatic Control, Vol. AC-24, No. 4, August 1979.

[8] A. Emami-Naeini and S. Rock, "On Asymptotic Behavior of Non-Square Optimal Regulators", *Proceedings of the 23rd Conference on Decision and Control*, Las Vegas, NV, December 1984.

[9] Ly,Uy Loi, "A Design Algorithm For Robust Low-Order Controllers", Ph.D. Thesis, Department of Aeronautics and Astronautics, Stanford University, SUDAAR No. 536, November 1982.

[10] , "Experiments in End-Point Control of Manipulators with Elastic Drives", Ph.D. Thesis, Department of Aeronautics and Astronautics, SUDAAR No. 568, May 1988.

[11] B.T. Resenauer, M.J. Balas and M.F. Ramey, "Reduced-Order Model Based Control of Large Flexible Manipulators: Theory and Experiment", *Proceedings of the 1990 American Control Conference*, May 1990, pp. 1760-1765.

[12] S.A. Collins and al., "Design, Manufacture, and Application to Space Robotics of Distributed Piezoelectric Film Sensors", *Proceedings of the 1990 AIAA Structures, Design and Material Conference*, April 1990.

[13] The MathWorks, Inc., 21 Eliot Street, So. Natick, MA 01760, *MATLAB^{TM} User's Guide*, 1989.

[14] Integrated Systems, Inc., 2500 Mission College Blvd., Santa Clara, CA, 95054, *MATRIXx^{TM} User's Guide*, 1990.

[15] D.B. Schaechter and D.A. Levinson, "Interactive Computerized Symbolic Dynamics for the Dynamicist", Proceedings of the 1988 American Control Conference, Atlanta, GA, June 15-17 1988.

Appendix A

Personnel and Interactions with Research Community

This appendix gives the list of professional personnel and the interactions with the research community in the context of the current contract.

A.1 Personnel

Principal investigator:

Dr. Eric Schmitz is a staff engineer in the Robotics Research and Technology Department and also an adjunct professor in the Aerospace Engineering Department at the University of Colorado at Boulder. Dr. Schmitz obtained his Ph.D.degree in aeronautics and astronautics from Stanford University in June 1985. The title of his doctoral thesis is "Experiments on the end-point position control of a very flexible one-link manipulator".

Research team:

Madison F. Ramey is a senior engineer in the Robotics Research and Technology Department. He obtained his M.S. degree in the Department of Mechanical Engineering at Purdue University in May 1986.

Rodney Beeston and Scott Mickey of the Robotics Research and Technology have been instrumental in the integration of the experimental testbed (originally designed by Phil Brunson, Paul Cogeos and Wes Mahoney).

A.2 Papers Presented at Conferences

The following papers have been presented at conferences.

1. Eric Schmitz, " Modeling and Control of a Planar Manipulator with an Elastic Forearm ", Proceedings of the 1989 IEEE International Conference on Robotics

and Automation, pp. 894-899, Scottsdale, Arizona

2. Eric Schmitz and Madison Ramey, " A Simplified Dynamic Model for an Experimental Planar Manipulator with an Elastic Forearm", presented at the 1989 American Conference, Pittsburgh, PA.

3. Madison Ramey and Eric Schmitz, " LQR Design for an Experimental Planar Elastic Arm with a Large Tip Payload", Proceedings of the 1990 American Conference, pp. 1729-1732 San Diego, CA.

A.3 Interactions

We have been cooperating closely with Professor A. Von Flotow of the MIT Aeronautics and Astronautics Department. This activity has been formalized with a subcontract given to Professor Von Flotow under the Independent Research and Development program of the Robotics section of the Research and Technology Department (D75). Carlos Padilla, a Ph.D. candidate under the supervision of Professor Von Flotow, has spent three months at Martin Marietta (July-August 1989, January 1990) working on the development of control laws for the elastic arm testbed. Carlos also integrated his simulation code for the flexible arm with the MATRIXx/System-Build CAD software. Distributed vibrational mode sensors using piezoelectric material(PVDF) have been developed by Professor Von Flotow and his research team for the flexible arm testbed. Testing and validation of these new sensors were sucessfully performed last January and are reported in [12].

We have also been working with Professor M. Balas of the Department of Aerospace Engineering at University of Colorado at Boulder. The flexible arm tesbed has been used by Professor Balas to demonstrate the residual mode filter design technique on a single elastic link. The results of this work have been reported in [11]. Future work will address the implementation of an adaptive version of the residual mode filter.

Finally, two sessions on the subject of dynamics and control of elastic manipulators have been organized by E. Schmitz for the 1989 and 1990 American Control Conferences.

Appendix B

Simplified Mass and Stiffness Matrices for 3-D Elastic Structure

The derivation of the simplified mass and stiffness matrices for the articulated arm shown in Figure B.1 is given in this section. It is assumed that each link can bend along two orthogonal directions. Torsional deflections are neglected here. The equations of motion are derived by keeping only the nonlinear terms involving the rigid-body generalized coordinates X_r and $\dot{X}_r$. Referring to equation (2-3) of Section 2.2 of the report, this is equivalent to computing the "simplified" mass matrix $\overline{M}(X_r)$ and stiffness matrix K. The mass matrix and the stiffness matrix are written as:

$$\overline{M} = \begin{bmatrix} \overline{M}_{RR} & \overline{M}_{RE} \\ \overline{M}_{RE}{}^{T} & \overline{M}_{EE} \end{bmatrix} \tag{B-1}$$

$$K = \begin{bmatrix} 0 & 0 \\ 0^{T} & K_{EE} \end{bmatrix} \tag{B-2}$$

The rigid-body mass matrix $\overline{M}_{RR}$ can be readily derived for the 3 DOF rigid structure where the two main links are assumed to be rigid. Symbolic calculators for rigid body dynamics applications such as [15] can be used for that purpose. Therefore the sections below discusses only the derivation of matrices $\overline{M}_{RE}$, $\overline{M}_{EE}$ and K_{EE}.

B.1 Kinematics

The inertial frame R_0 is defined as $(S, \underline{i}_0, \underline{j}_0, \underline{k}_0)$, as shown in Figure B-1. Frames R_1, R_2 and R_3 are attached to each body respectively at each articulation. The shoulder and elbow links are tangent to the vectors $\underline{i}_2$ and $\underline{i}_3$ respectively in the frames R_2 and R_3. Frame R_1 is obtained from R_0 by a simple rotation $\tilde{R}(\underline{k}_0, \theta_1)$. Frame R_2 is obtained from R_1 by the simple rotation $\tilde{R}(-\underline{j}_1, \theta_2)$. Frame R_{t2} is attached to the elbow articulation E with $\underline{i}_{t2}$ tangent to the first link. R_{t2} is related to R_2 by the following direction cosine matrix:

$$\begin{bmatrix} \underline{i}_{t2} \\ \underline{j}_{t2} \\ \underline{k}_{t2} \end{bmatrix} = \begin{bmatrix} 1 & \frac{\partial v_s}{\partial x}(l) & \frac{\partial w_s}{\partial x}(l) \\ -\frac{\partial v_s}{\partial x}(l) & 1 & 0 \\ -\frac{\partial w_s}{\partial x}(l) & 0 & 1 \end{bmatrix} \begin{bmatrix} \underline{i}_2 \\ \underline{j}_2 \\ \underline{k}_2 \end{bmatrix} \tag{B-3}$$

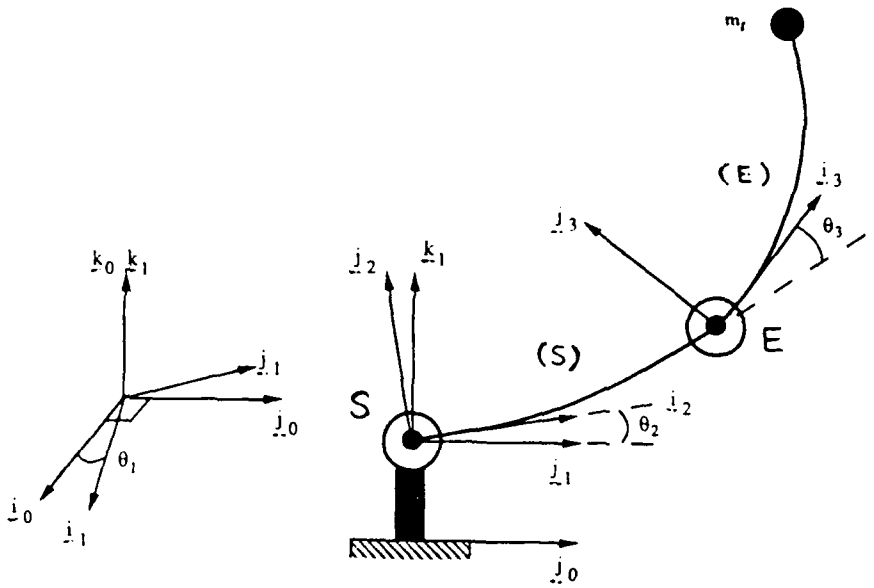

Figure B-1: Schematic of the 3-D elastic articulated structure

where v_s and w_s are defined below as the two bending coordinates for the shoulder link (S). The direction cosine matrix is derived with the assumption that the elastic deflections and slopes are first-order quantities.

Finally frame R_3 is obtained from R_{t2} by a simple rotation $\tilde{R}(\underline{k}_{t2}, \theta_3)$. Note that l is the length of the 2 main links.

The location of a current point M_s along the neutral axis of the shoulder link (S) is defined in R_2 by the displacement vector $\mathbf{r_s}$:

$$\underline{r}_s = x_s \underline{i}_2 + v_s(x_s, t)\underline{j}_2 + w_s(x_s, t)\underline{k}_2 \qquad (B-4)$$

Similarly, the location of a current point M_e along the neutral axis of the elbow link (E) is defined in R_3 by the displacement vector $\mathbf{r_e}$:

$$\underline{r}_e = x_e \underline{i}_3 + v_e(x_e, t)\underline{j}_3 + w_e(x_e, t)\underline{k}_3 \qquad (B-5)$$

For both cases, we have neglected the second-order axial deformations due to the forshortening effects. Each link has the same length l.

From (B-4) and (B-5), the velocity of the current point along links (S) and (E) are given as:

$$\mathbf{V_{M_s}} = \omega_2 \times \underline{r}_s + \frac{\mathbf{d}}{\mathbf{dt}}^{\mathbf{R_2}} \underline{r}_s^{el} \qquad (B-6)$$

$$\mathbf{V_{Me}} = \mathbf{V_E} + \omega_3 \times \underline{r}_e + \frac{d}{dt}^{R_3} \underline{r}_e^{el} \tag{B-7}$$

where $\underline{r}_s^{el}$ and $\underline{r}_e^{el}$ are the elastic part of the displacement vectors $\underline{r}_s$ and $\underline{r}_e$ respectively; $\mathbf{V_E}$ is the absolute velocity of the elbow joint (modelled as a lumped mass).

The inertial angular velocities ω_2 and ω_3 are expressed as:

$$\begin{aligned} \omega_2 &= \dot{\theta}_1 \underline{k}_0 + \dot{\theta}_2 \underline{k}_2 \\ \omega_3 &= \omega_2 + \frac{\partial^2 \mathbf{v_s}}{\partial \mathbf{x} \partial \mathbf{t}}(\mathbf{L}) \underline{k}_2 - \frac{\partial^2 \mathbf{w_s}}{\partial \mathbf{x} \partial \mathbf{t}}(\mathbf{L}) \underline{j}_2 + \dot{\theta}_3 \underline{k}_3 \end{aligned} \tag{B-8}$$

B.2 Linearized Partial Velocities

Using the assumed-modes method, the elastic deflections $v_s(x,t)$, $w_s(x,t)$, $v_e(x,t)$ and $w_e(x,t)$ are expressed in terms of the series:

$$v_s(x,t) = \mathbf{\Phi}^t_{\mathbf{v_s}}(\mathbf{x})\mathbf{Q_s}(\mathbf{t});\ \mathbf{w_s}(\mathbf{x},\mathbf{t}) = \mathbf{\Phi}^t_{\mathbf{w_s}}(\mathbf{x})\mathbf{R_s}(\mathbf{t}) \tag{B-9}$$

$$v_e(x,t) = \mathbf{\Phi}^t_{\mathbf{v_e}}(\mathbf{x})\mathbf{Q_e}(\mathbf{t});\ \mathbf{w_e}(\mathbf{x},\mathbf{t} = \mathbf{\Phi}^t_{\mathbf{w_e}}(\mathbf{x})\mathbf{R_e}(\mathbf{t}) \tag{B-10}$$

where $\mathbf{Q_s(t)}$, $\mathbf{Q_e(t)}$,$\mathbf{R_s(t)}$ and $\mathbf{R_e(t)}$ are four vectors of n modal coordinates; $\mathbf{\Phi_{v_s}(x)}$,$\mathbf{\Phi_{w_s}(x)}$, $\mathbf{\Phi_{v_e}(x)}$ and $\mathbf{\Phi_{w_e}(x)}$ are four vectors of n assumed mode shapes.

The velocity $\mathbf{V_M}$ for a point along the shoulder or elbow link can be written as:

$$\mathbf{V_M} = \mathbf{G_M}\,\dot{\mathbf{X}} \tag{B - 11}$$

where $\mathbf{G_M}$ is a row vector of $3+4n$ partial velocities. The kth term of $\mathbf{G_M}$ is the partial velocity $\mathbf{G^k_M}$ with respect to the kth generalized coordinate. The row vector $\mathbf{G_M}$ can be expressed as the sum of two vectors:

$$\mathbf{G_M} = \overline{\mathbf{G}}_\mathbf{M}(\mathbf{X_r},\underline{\mathbf{0}}) + \tilde{\mathbf{G}}_\mathbf{M}(\mathbf{X_r},\mathbf{X_{el}}) \tag{B - 12}$$

In order to obtain the *simplified* dynamic model as defined in Section 2.1, only the row vector $\overline{\mathbf{G}}_\mathbf{M}$ need to be computed.

Accordingly, after partioning in terms of rigid and elastic coordinates, the row vector of partial velocities are given as:

$$\overline{G}_M^{s\ rig} = [\underline{k}_1 \times x_s \underline{i}_2, \underline{k}_2 \times x_s \underline{i}_2, \underline{0}] \quad \text{(B-13)}$$

$$\overline{G}_M^{s\ el} = \left[\Phi_{vs}\underline{j}_2, \Phi_{ws}\underline{k}_2, \underline{0}, \underline{0}\right] \quad \text{(B-14)}$$

$$\overline{G}_M^{e\ rig} = \left[\underline{k}_1 \times \underline{r}_{se}^{rig}, \underline{k}_2 \times \underline{r}_{se}^{rig}, \underline{k}_3 \times x_e \underline{i}_3\right] \quad \text{(B-15)}$$

$$\overline{G}_M^{e\ el} = \left[\underline{g}_{v_s}^e, \underline{g}_{w_s}^e, \Phi_{ve}\underline{j}_3, \Phi_{we}\underline{k}_3\right] \quad \text{(B-16)}$$

with the follwing definitions:

$$\underline{r}_{se}^{rig} = L\underline{i}_2 + x_e\underline{i}_3 \quad \text{(B-17)}$$

$$\underline{g}_{v_s}^e = \frac{d\Phi_{vs}}{dx}(l)\,\underline{k}_2 \times x_e\underline{i}_3 + \Phi_{vs}(l)\underline{j}_2 \quad \text{(B-18)}$$

$$\underline{g}_{w_s}^e = -\frac{d\Phi_{ws}}{dx}(l)\,\underline{j}_2 \times x_e\underline{i}_3 + \Phi_{ws}(l)\underline{k}_2 \quad \text{(B-19)}$$

B.3 Mass Matrix $\overline{M}(X_r)$

The elements of the mass matrix $\overline{M}$ are expressed as:

$$\overline{m}_{rs} = \sum_{i=1}^{3} \int_{B_i} \overline{G}_{M_i}^{r} \cdot \overline{G}_{M_i}^{s} dm \quad \text{(B - 20)}$$

where $\overline{G}_i^r$ is the rth partial velocity of a current point belonging to body B_i. The submatrices $\overline{M}_{RE}$ and $\overline{M}_{EE}$ are obtained by forming scalar products of partial velocities for material points along the two elastic links.

B.3.1 Submatrix $\overline{M}_{RE}$

Using equation (B-20) together with equations (B-13) to (B-16), the $3 \times 4n$ rigid/elastic coupling mass matrix $\overline{M}_{RE}$ is given as:

$$\begin{bmatrix} \underline{0} & -c_2\mathbf{H}_{ws} + \mathbf{f}_{12} & \underline{0} & -lc_2\mathbf{P}_{we} - c_{(2+3)}\mathbf{H}_{we} \\ \mathbf{H}_{vs} + \mathbf{f}_{21} & \underline{0} & Lc_3\mathbf{P}_{ve} + \mathbf{H}_{ve} & \underline{0} \\ \mathbf{f}_{31} & \underline{0} & \mathbf{H}_{ve} & \underline{0} \end{bmatrix} \quad \text{(B - 21)}$$

where c_2 is a short notation for $\cos\theta_2$; $\underline{\mathbf{P}}_v, \underline{\mathbf{P}}_w, \underline{\mathbf{H}}_v$ and $\underline{\mathbf{H}}_w$ are $1 \times n$ row vectors of integrals of the assumed mode shapes computed along each elastic link (B):

$$\mathbf{P_v} = \int_B \mathbf{\Phi_v(x)dm} \tag{B-22}$$

$$\mathbf{P_w} = \int_B \mathbf{\Phi_w(x)dm} \tag{B-23}$$

$$\mathbf{H_v} = \int_B x\mathbf{\Phi_v(x)dm} \tag{B-24}$$

$$\mathbf{H_w} = \int_B x\mathbf{\Phi_w(x)dm} \tag{B-25}$$

The intermediate row vectors $\mathbf{f_{12}}$,$\mathbf{f_{21}}$ and $\mathbf{f_{31}}$ are:

$$\mathbf{f_{12}} = -c_3\frac{d\mathbf{\Phi_{ws}}}{\mathbf{dx}}(l)\,[m_e a_e l c_2 + I_e c_{(2+3)}] - m_e\mathbf{\Phi_{ws}}(\mathbf{l})\,[\mathbf{lc_2} + \mathbf{a_e c_{(2+3)}}] \tag{B-26}$$

$$\mathbf{f_{21}} = \frac{d\mathbf{\Phi_{vs}}}{\mathbf{dx}}(l)\,[m_e a_e l c_3 + I_e] + m_e[l + a_e c_3]\mathbf{\Phi_{vs}}(\mathbf{l}) \tag{B-27}$$

$$\mathbf{f_{31}} = m_e a_e \mathbf{\Phi_{vs}}(\mathbf{l}) + \mathbf{I_e}\frac{\mathbf{d\Phi_{vs}}}{\mathbf{dx}}(\mathbf{l}) \tag{B-28}$$

where m_e is the mass of link (E) and a_e is the distance from joint E to the center of mass of the undeformed link (E).

B.3.2 Submatrix $\overline{M}_{EE}$

From Eq. (B-20), the submatrix $\overline{M}_{EE}$ is made of four block diagonal submatrices given as:

$$M_{EE}^{v_s v_s} = \int_S \mathbf{\Phi_{vs}}^{\mathbf{T}}(\mathbf{x})\mathbf{\Phi_{vs}(x)}\,\mathbf{dm} + \mathbf{M_1} \tag{B-29}$$

$$M_{EE}^{w_s w_s} = \int_S \mathbf{\Phi_{ws}}^{\mathbf{T}}(\mathbf{x})\mathbf{\Phi_{ws}(x)}\,\mathbf{dm} + \mathbf{M_2} \tag{B-30}$$

$$M_{EE}^{v_e v_e} = \int_E \mathbf{\Phi_{ve}}^{\mathbf{T}}(\mathbf{x})\mathbf{\Phi_{ve}(x)}\,\mathbf{dm} \tag{B-31}$$

$$M_{EE}^{w_e w_e} = \int_E \mathbf{\Phi_{we}}^{\mathbf{T}}(\mathbf{x})\mathbf{\Phi_{we}(x)}\,\mathbf{dm} \tag{B-32}$$

where (B) refers to a given elastic link and the two intermediate matrices M_1 and M_2 are given as:

$$M_1 = m_e\mathbf{\Phi_{vs}}^{\mathbf{T}}(\mathbf{l})\mathbf{\Phi_{vs}(l)} + \mathbf{2m_e a_e}\frac{\mathbf{d\Phi_{vs}}}{\mathbf{dx}}^{\mathbf{T}}(\mathbf{l})\mathbf{\Phi_{vs}(l)} + \mathbf{I_e}\frac{\mathbf{d\Phi_{vs}}}{\mathbf{dx}}^{\mathbf{T}}(\mathbf{l})\frac{\mathbf{d\Phi_{vs}}}{\mathbf{dx}}(\mathbf{l})$$

$$M_2 = m_e\mathbf{\Phi_{ws}}^{\mathbf{T}}(\mathbf{l})\mathbf{\Phi_{ws}(l)} + \mathbf{2m_e a_e c_3}\frac{\mathbf{d\Phi_{ws}}}{\mathbf{dx}}^{\mathbf{T}}(\mathbf{l})\mathbf{\Phi_{ws}(l)} + \mathbf{I_e c_3^2}\frac{\mathbf{d\Phi_{ws}}}{\mathbf{dx}}^{\mathbf{T}}(\mathbf{l})\frac{\mathbf{d\Phi_{ws}}}{\mathbf{dx}}(\mathbf{l})$$

B.4 Stiffness Matrix K_{EE}

The elements of the stiffness matrix are obtained from the expression for the elastic potential energy:

$$V_{el} = \sum_{i=1}^{i=2} \int_{B_i} \left[EI^i_{zz} \left(\frac{\partial^2 v_i}{\partial x^2} \right)^2 + EI^i_{yy} \left(\frac{\partial^2 w_i}{\partial x^2} \right)^2 \right] dx \qquad (B-33)$$

where EI_{zz} and EI_{yy} are the bending stiffness for deflections along y and z axes.

From the series (B-9) and (B-10), the stiffness matrix are make of 2 sets of block diagonal sub matrices of the form:

$$K_{vv} = \int_B EI_{zz} \frac{d^2 \Phi_v}{dx^2}^T (x) \frac{d^2 \Phi_v}{dx^2}(x)\, dx \qquad (B-34)$$

$$K_{ww} = \int_B EI_{yy} \frac{d^2 \Phi_w}{dx^2}^T (x) \frac{d^2 \Phi_w}{dx^2}(x)\, dx \qquad (B-35)$$

where (B) refers to a given elastic link.

Appendix C

MATRIXx UDF's and Control Law Subroutines

In this appendix, we provide some of the MATRIXx UDF's (User-Defined Functions) developed to help automate the LQG controller design/analysis, and the C-code listing of a module which implements a control law for the 2DOF arm.

C.1 LQG Design and Analysis UDF's

The first two UDF's, `RegLocus`, and `EstLocus` are used to generate, respectivley, the optimal regulator and estimator loci presented in chapter 3. In generating these loci, the UDF's `RegTz` and `EstTz` are used to compute the finite zeros (asymptotic closed-loop pole locations) for a given regulator and estimator design respectively.

RegLocus.UDF

```
//  [ Ev_Reg, Tz_Reg, Kr_Reg ] = RegLocus( S, Ns, Q, R, Rho, Popt )
//
//  MATRIXx function to generate the optimal regulator root locus versus the
//  control weighting rho.  For each value of rho in  the vector Rho,
//  Lqrlocus returns the regulator poles (Ev_Reg) and full-state feedback
//  gain vectors (Kr_Reg).  As rho goes to zero, the regulator poles go to
//  the finite zeros (Tz_Reg) as dictated by Q.
//
//  Performance index assumed:
//
//        J = Integral{ z'*diag(Q)*z + u'*rho*diag(R)*u } dt
//
//    where:  z = Cx are the plant outputs to be regulated
//            C = the output matrix given in S.
//
//  Inputs:
//
//    S     :=  Plant dynamics matrix,  S = [ A B ; C 0 ]
//    Ns    :=  Plant order
//    Q     :=  Row vector of output weightings
//    R     :=  Row vector of input weightings
//    Rho   :=  Vector of control weightings, rho
//    Popt  :=  String of PLOT command plotting options; if Popt
//              is not specified, the root-locus is not displayed.
//              (e.g., Popt = 'xmin=-20 xmax=0 ymin=0 ymax=20 ...')
//
//  Outputs:
```

```
//
//    Ev_Reg := Matrix whose columns contain the regulator poles
//              for each value in Rho.
//    Tz_Reg := Vector of the regulator finite zeros.
//    Kr_Reg := Matrix of Regulator gain vectors for each value of Rho.
//              To extract the regulator gains Kri for Rho(i), type:
//                   Kri = Kr_Reg([ Nact*i-1, Nact*i ],:)
//              where Nact = number of actuators in B.

//  Author:   M. F. Ramey, Martin Marietta Astronautics, R&T Group

[ A, B, C, D] = split( S, Ns );

[Nsens,Nact] = size(D);
Nq = max(size(Q));
Nev = max(size(Rho));

// Do some simple error checking:
if Nq<>Nsens, ...
   display('Error: # of Output Weightings in Q .ne. # of Outputs in C');...
   retf;...
end;

// Compute the finite regulator zeros:
Tz_Reg = Tzreg(S,Ns,Q);

// Convert the output weightings to state weightings:
Qxx  = C' * diag(Q) * C;

// Form the input weighting matrix:
Ruu0 = diag(R);

// Begin the iterations on Rho:
Ruu = Rho(1)*Ruu0;     // First iteration
[ Ev_Reg, Kr_Reg ] = regulator( A, B, Qxx, Ruu );

for i=2:Nev, ...      // Remaining iterations
 Ruu = Rho(i)*Ruu0; ...
 [ Evi, Kri ] = regulator( A, B, Qxx, Ruu ); ...
 Ev_Reg = [ Ev_Reg , Evi ]; ...
 Kr_Reg  = [ Kr_Reg ; Kri ]; ...
end;

// If Plotting options are specified, Do plotting:
if exist('Popt')=1,...
   plot(real(Ev_Reg),imag(Ev_Reg),...
        ['xlab/Real/ ylab/Imaginary/symbol mark 3' Popt]); ...
   plot(real(Tz_Reg),imag(Tz_Reg),'symbol mark 2 keep'); ...
end;

// Finis.
retf
```

EstLocus.UDF

```
//  [ Ev_Est, Tz_Est, Ke_Est ] = EstLocus( S, Ns, Kq, Mu, Popt )
//
//  MATRIXx function to generate the optimal estimator root-locus versus
//  Kq, the process noise noise intensities.  Returns the estimator eigenvalues
//  (Ev_Est) and gains (Ke_Est) for each value of Kq.  As Kq goes to infinity,
//  the estimator poles will go to the finite estimator zeros (Tz_Est)
```

```
//  dictated by Mu.
//
//  Inputs:
//
//    S    := Continuous-time plant matrix S = [ A B ; C 0 ]
//    Ns   := Order of S
//    Mu   := Vector of measurement noise intensities such that
//            the measurement noise covariance matrix Qyy is:
//            Qyy = diag( Mu**(-1) );  The elements of Mu can be
//            interpreted as the noise intensity ratios of primary_sensor(s)-
//            to-auxilliary_sensors(s) (mu = R_prim/R_aux).
//    Kq   := Vector of process noise intensities
//    Popt := Optional string of PLOT command plotting options.
//            (e.g., Popt = 'xmin=-20 xmax=0 ymin=0 ymax=20 ... ')
//            If Popt is not specified, the root-locus is not displayed.
//
//  Outputs:
//
//    Ev_Est := Matrix whose columns contain the estimator eigen values for
//              each value of Kq.
//    Tz_Est := Vector of finite estimator zeros.
//    Ke_Est := Matrix of estimator gains for each value of Kq.
//              To extract the estimator gains Kej for Kq(j), type:
//                   Kej = Ke_Est(:,[ Ny*j-1, Ny*j ])

//  Author:  M. F. Ramey, Martin Marietta Astronautics, R&T Group

[ A, B, C, D ] = split( S, Ns );

[Nsens,Nact]=size(D);
Nmu = max(size( Mu ));
Nev = max(size( Kq ));

// Do some simple error checking:
if Nmu<>Nsens, ...
   display('Error: # of Ratios in Mu <> # of Sensors in C');...
   retf;...
end;

// Form the process noise intensity matrix:
q    = eye(Nact);            // Equal weightings on actuators!
Qxx0 = B*q*B';

// Form the measurement noise intensity matrix:
Qyy  = diag( Mu**(-1) );

// Compute the finite estimator 'zeros':
Tz_Est = Tzest(S,Ns,Mu);

// Begin iterations on process noise intensities Kq:

Qxx = Kq(1)*Qxx0;          // First Iteration
[ Ev_Est, Ke_Est ] = estimator( A, C, Qxx, Qyy ); ...

for j=2:Nev, ...           // Remaining Iterations
  Qxx = Kq(j)*Qxx0; ...
  [ Evi, Kei ] = estimator( A, C, Qxx, Qyy ); ...
  Ev_Est = [ Ev_Est, Evi ]; ...
  Ke_Est = [ Ke_Est,  Kei ]; ...
end;

// If Plotting options are specified, Do plotting:
if exist('Popt')=1,...
   plot(real(Ev_Est),imag(Ev_Est),...
```

```
        ['xlab/Real/ ylab/Imaginary/symbol mark 3 ' Popt]); ...
   plot(real(Tz_Est),imag(Tz_Est),'symbol mark 2 keep'); ...
end;

// Finis.
retf
```

RegTz.UDF

```
//  Tz_Reg = RegTz( S, Ns, Q );
//
//  Returns Tz_Reg, the finite regulator 'transmission' zeros
//  for the given plant S = [ A, B ; C, 0 ] with output weightings Q.
//
//  Performance index assumed:
//
//        J = Integral[ z'*diag(Q)*z + u'*rho*diag(R)*u ] dt
//
//    where:  z = Cx are the plant outputs to be regulated
//            C = the output matrix given in S.
//
//  Inputs:
//
//    S     :=  Plant dynamics matrix,  S = [ A B ; C 0 ]
//    Ns    :=  Plant order
//    Q     :=  Row vector of output weightings
//
//  Outputs:
//
//    Tz_Reg := Vector of the regulator finite zeros.
//
[ A, B, C, D ] = split( S, Ns );
[Nsen,Nact]=size(D);

//  Convert the output weightings to state weightnings:
Qxx  = C' * diag(Q) * C;

Aaug = [ A, 0*ones(Ns,Ns); Qxx, -A' ];
Baug = [ B; 0*ones(Ns,Nact) ];
Caug = [ 0*ones(Nact,Ns), -B' ];

// Retain only the Left-Half Plane Zeros:
Tz_Reg = sortval(zeros([Aaug,Baug;Caug,0*ones(Nact,Nact)],2*Ns));
Nz = max(size(Tz_Reg))/2;
Tz_Reg = Tz_Reg(1:Nz);

// Finis
retf
```

EstTz.UDF

```
//  Tz_Est = EstTz( S, Ns, Mu )
//
//  MATRIXx function that returns a vector of finite
//  estimator 'transmission' zeros for the given values of Mu.
//
//  S    := Continuous-time plant S = [ A, B; C 0 ];
//  Ns   := Order of S
```

```
//  Mu    := Vector of measurement noise intensities such that
//           the measurement noise covariance matrix Qyy is:
//           Qyy = diag( Mu**(-1) )

[ A, B, C, D ] = split( S, Ns );
[Nsens,Nact] = size( D );

XX = C' * diag(Mu) * C ;
Atild = [ A, 0*ones(Ns,Ns) ; XX, -A' ];
Btild = [ B; 0*ones(Ns,Nact) ];
Ctild = [ 0*ones(Nact,Ns), -B' ];
Dtild = 0.0*ones(Nact,Nact);

Tz_Est = zeros([Atild,Btild;Ctild,Dtild], 2*Ns );

// Retain only the Left-Half Plane zeros:
Nz = max(size(Tz_est))/2;
Tz_Est = sortval(Tz_Est);
Tz_Est = Tz_est(1:Nz);

// Finis.
retf
```

C.2 Real-Time Controller Module

Here we list the C-code for a generic compensator with 5 sensor inputs and 2 actuator output commands. The structure of the controller is as follows:

$$\begin{aligned} z(k+1) &= A_c z(k) + B_c e(k) \\ u(k+1) &= C_c z(k) + D_c e(k) \end{aligned}$$

where (A_c, B_c, C_c, D_c) are the compensator matrices, z is the state-vector, u is the vector of torque commands, and $e(k) = [y_{ref}(k) - y_{meas}(k)]$ is the error between the reference values and the measured values.

GenComp.c

```
#include <stdio.h>
#include "mfr_mult.h"

/*=============================================================================
MODULE NAME:   GenComp
    VERSION:   1.0

PURPOSE:
   This module provides a control law for the Flexible Manipulator Testbed.
   It consists of a generic state-space compensator (up to 10th-Order) of
   the following form:

         x(k+1) = A*x(k) + B*e(k)
         u(k+1) = C*x(k) + D*e(k)
```

```
   where (A,B,C,D) are the compensator matrices, x is the state vector,
   u is the control vector, and e is the error between the reference
   commands and the measured signals.

   As inputs, the compensator uses the 5 sensor measurements defined for
   the Joint Resolvers (2), Joint Tachometers (2), and the two Strain
   channels (2), the previous sample's actuator command, and the Shoulder and
   Elbow Position/Velocity reference commands.
   The estimator takes the error signals e(k) as input.

   As output, this control law computes joint torque commands for the Shoulder
   and Elbow actuators in Newton-meters.  Any additional feedforward filtering
   and limiting of the PWM voltage signals is done by the calling routine.

   Also note that this control law allows the user to "tweak" loop gains
   via an interactive query during the real-time initialization.

   The matrices (A,B,C,D) and any other real-type parameters  are stored
   in the Real_Params_Str structure.  The sensor inputs are stored in the
   Sensor_Data_Str structure.  The control commands are stored in the
   Cmnd_Str structure.  Any integer parameters are stored in the
   Int_Param_Str structure.

PROCEDURES WITHIN THIS MODULE
   Init_Control_Law             : Sets up the control law.

   Control_Law_1                : Updates the control commands

   Control_Law_2                : Updates the compensator states (after I/O)

   Close_Control_Law            : Cleans up the control law (usually empty).

PROGRAMMER NAME: Madison F. Ramey
================================================================================*/
/* Variables global to this module:                                            */

#include   "genlqg.h"          /* All #define and struct definitions!          */
#include   "flex.h"

/*==============================================================================
PROCEDURE NAME: Init_Control_Law

PURPOSE:
   This procedure initializes the compensator's state and control vectors,
   and queries the user for loop tweaking gains.

================================================================================*/
void Init_Control_Law(Rp, Ip)

   Real_Params_Str         *Rp;
   Int_Params_Str          *Ip;

{
   int       i;
   char      ans;
   static    char *portname[NKTW] = {
             "Shldr Loop Gain",
             "Elbow Loop Gain"
             };

/* Set Default Values for Tweaking Gains and Query user:  */

   for ( i=0 ; i<NKTW ; i++ )
     K_twk[i] = 1.0;
```

```
    printf( "Do you want to tweak loop gains? (Y/N) ");
    do {
        ans = getchar();
    } while ((ans != 'Y') && (ans != 'N') && (ans != 'y') && (ans != 'n'));

    if ( ans == 'Y' || ans == 'y' ) {
       for ( i=0 ; i<=2 ; i++ ) {
         printf( "Enter Tweak Gain for %25s: ", portname[i]);
         scanf( "%f", &K_twk[i] );
       }
    }
    for ( i=0 ; i<NKTW ; i++ )
      printf( "%24s Gain:  %f \n", portname[i], K_twk[i] );

/* Initialize Compensator States: */

    for ( i=0 ; i<NX ; i++ )
      X_hat[i] = 0.0;

/* Initialize Compensator Inputs: */

    for ( i=0 ; i<NSEN ; i++ )
      Y_err[i] = 0.0;

/* Initialize Full-State Feedback Terms: */

    for ( i=0 ; i<NACT ; i++ )
      Cx[i] = 0.0;

} /* End of procedure Init_Control_Law */

/*=============================================================================
PROCEDURE NAME: Control_Law_1
       VERSION: 1.0

PURPOSE:
   This control law is executed immediately after the sensors are read.

=============================================================================*/

void Control_Law_1(Run_Time, Reference, Sensors,
                   Rp, Ip, Command, Err)

   float                    *Run_Time;
   Ref_State_Str            *Reference;
   Sensor_Data_Str          *Sensors;
   Real_Params_Str          *Rp;
   Int_Params_Str           *Ip;
   Cmnd_Str                 *Command;
   unsigned short int       *Err;              /* 16-bit word */

{
   float      De     [NACT];   /* Direct Transmission Terms */
   float      U_cmd  [NACT];   /* Output Torque Command */

/* Set the error signals:  */
/* (note that Shoulder Velocity Ref is scaled by its Gear ratio of 20) */

   Y_err[0] = -Sensors->Resolver[SH]    + Reference->Joint_Position[SH];
   Y_err[1] = -Sensors->Resolver[EL]    + Reference->Joint_Position[EL];
   Y_err[2] = -Sensors->Tachometer[SH] + Reference->Joint_Velocity[SH]*20.0;
   Y_err[3] = -Sensors->Tachometer[EL] + Reference->Joint_Velocity[EL];
   Y_err[4] = -Sensors->Strain[SH];
```

```
   Y_err[5] = -Sensors->Strain[EL];

/* Compute De, the direct-transmission terms:

   Multiply_NACTxNSEN_by_NSENx1 ( Rp->D_mtx, Y_err, De );

/* Command Torque U = Cx + Du where Cx is computed previously in Control_Law_2.

   U_cmd[SH] = Cx[0] + De[0];
   U_cmd[EL] = Cx[1] + De[1];

/* Transfer to Control Command Structure: */

   Command->Control_Command[SH] = U_cmd[SH]*K_twk[0];
   Command->Control_Command[EL] = U_cmd[EL]*K_twk[1];

   *Err = 0;

} /* End of procedure Control_Law_1 */


/*============================================================================
PROCEDURE NAME: Control_Law_2
       VERSION:

PURPOSE:
   This procedure does any computation after the torque command is sent to
   the arm.  Everything here is computed at the end of each frame.

   For the GenComp controller, here 1) we update the state estimate using
   the linear state-transition matrix and 2) compute the full-state feedback
   terms (Cx) needed for the next sample.

============================================================================*/

void Control_Law_2(Run_Time, Reference, Sensors,
                   Rp, Ip, Command, Err)

   float                  *Run_Time;
   Ref_State_Str          *Reference;
   Sensor_Data_Str        *Sensors;
   Real_Params_Str        *Rp;
   Int_Params_Str         *Ip;
   Cmnd_Str               *Command;
   unsigned short int     *Err;              /* 16-bit word */

{
   float      Ax        [NX];      /* Acomp * X_hat                        */
   float      Be        [NX];      /* Bcomp * Y_err                        */
   int        i             ;      /* Generic Index                        */

/*---- Calculate the next state estimate : -------

   Multiply_NXxNX_by_NXx1 ( Rp->Acomp, X_hat, Ax );
   Multiply_NXxNSEN_by_NSENx1 ( Rp->Bcomp, Y_err, Be );

   for ( i=0 ; i<NX ; i++ )
       X_hat[i] = Ax[i] + Be[i];

/*  Calculate Full State Feedback Terms Cx for Next Sample: */

   Multiply_NACTxNX_by_NXx1 ( Rp->Ccomp, X_hat, Cx );

} /* End of procedure Control_Law_2 */
```

```
/*==========================================================================
PROCEDURE NAME: Close_Control_Law
       VERSION:

PURPOSE:
   This procedure will clean up anything necessary after completion of a
   real-time run.

   This is not needed for the Generic LQG controller.
==========================================================================*/

void Close_Control_Law(Rp, Ip)

   Real_Params_Str         *Rp;
   Int_Params_Str          *Ip;

{
} /* End of procedure Close_Control_Law */
```